



# City Research Online

## City St George's, University of London

**Citation:** Li, Q., Stavropoulos-Vasilakis, E., Koukouvinis, P., Gavaises, M. & Bruecker, C. (2021). Micro-pillar sensor based wall-shear mapping in pulsating flows: In-Situ calibration and measurements in an aortic heart-valve tester. *Journal of Fluids and Structures*, 105, 103346. doi: 10.1016/j.jfluidstructs.2021.103346

This is the accepted version of the paper.

This version of the publication may differ from the final published version. To cite this item please consult the publisher's version.

**Permanent repository link:** <https://openaccess.city.ac.uk/id/eprint/26351/>

**Link to published version:** <https://doi.org/10.1016/j.jfluidstructs.2021.103346>

**Copyright and Reuse:** Copyright and Moral Rights remain with the author(s) and/or copyright holders. Copies of full items can be used for personal research or study, educational, or not-for-profit purposes without prior permission or charge, unless otherwise indicated, provided that the authors, title and full bibliographic details are credited, a hyperlink and/or URL is given for the original metadata page and the content is not changed in any way. For full details of reuse please refer to [City Research Online policy](#).

# Micro-pillar sensor based wall-shear mapping in pulsating flows: In-situ calibration and measurements in an aortic heart-valve tester

Qianhui Li<sup>1</sup>, Evangelos Stavropoulos-Vasilakis, Phoevos Koukouvinis,  
Manolis Gavaises and Christoph H. Bruecker

School of Mathematics, Computer Science and Engineering, City, University of London, Northampton Square,  
London, EC1V 0HB, UK

## Abstract

Accurate wall-shear stress (WSS) in-vitro measurements within complex geometries such as the human aortic arch under pulsatile flow are still difficult to achieve, meanwhile such data are important for classifying impacts of prosthetic valves on aortic walls. Micro-cantilever beams can serve to sense the WSS in such flows for applications in in-vitro flow tester. However, within pulsatile flows and complex 3D curved geometries such as the aortic arch, the flexible sensor structures are subject to oscillating boundary layer thickness and profile shape, which may not have been taken into account in the calibration procedure. The fluid-structure interaction is sensitive to these changes, thus reflecting also the flow-induced deflection of the sensor tip which is actually the sensing signal. We develop herein a methodology for in-situ calibration of the response of the sensors directly in the complex geometry of the aortic arch, assisted by reference data from numerical simulations of the flow under the same boundary conditions. For this procedure, a quick exchange of the heart valve in the tester with a tubular insert is done to provide a smooth contour in the curved aorta model. Arrays of 500 $\mu$ m long micro-pillar WSS sensors in the aorta model are calibrated under physiological pulsatile flow and used then for mapping the WSS evolution in the arch induced by two different heart valves, showing their difference of impact. The developed methodology completes the in-house built in-vitro flow tester with a reliable WSS measurement technique and provides a unique hydrodynamic testing facility for heart valve prostheses and their impact on the WSS distal along the aortic walls.

**Keywords:** wall shear stress, aorta, pulsating flow, micro-pillar sensors, CFD-assisted calibration, heart-valve tester

## 1. Introduction

The mean magnitude and fluctuation amplitude of wall shear stress (WSS) in the human circulatory flow system have important influence on possible vascular diseases. For instance, vessel segments exposed to low WSS or oscillating WSS has been reported to be at the highest risk for developing atherosclerosis (Chien et al., 1998; Shaaban and Duerinckx, 2000). Also, oscillating shear forces plus large WSS gradients were linked to the development of intimal hyperplasia (IH) (Haruguchi and Teraoka, 2003). Direct measurements of the WSS in the vessels are still difficult if not impossible in these complex geometries, therefore most of the data in literature are obtained from detailed velocity field measurements. However, because of limits in spatial and temporal resolution, the results of these measurements show larger variations and suffer from the lack of reliable means for validation against a standard reference (Katritsis et al., 2007). As reported by Potters et al. (Potters et al., 2014), values in the literature for cycle averaged aortic WSS differ over one order of magnitude.

WSS is generally obtained from the wall-normal gradient of the velocity component parallel to the wall. The underlying flow fields could typically be obtained in three ways: (i) in-vivo velocity measurements such as phase-contrast magnetic resonance imaging (PC-MRI) (Markl et al., 2011; Papathanasopoulou et al., 2003; Potters et al., 2014); (ii) in-vitro measurements, e.g. using optical transparent models and Volumetric Particle Image Velocimetry (V-PIV) methods, such as 3D Particle Tracking Velocimetry (3D-PTV), 3D Scanning-PIV or 3D Tomo-PIV (a review of such methods is given in (Raffel et al., 2018b)); (iii) numerical simulations using CFD, see (Gross-Hardt et al., 2018; Lantz et al., 2011; Orlü and Vinuesa, 2020) among many other.

Numerical studies on WSS in biological systems have been proven beneficial for conditions where experimental measurements are inaccessible, whereas it remains partly limited due to uncertainties in the boundary conditions, the extraction of the exact geometry of the blood vessels as well as the mesh sensitivity (Gross-Hardt et al., 2018); accurate calculation of the velocity gradients at the wall requires a high-resolution mesh at the near-wall region, which results to high computational cost. A typical Reynolds number in the aorta is of the order of 10,000; this requires high-performance computing power to achieve sufficient resolution down to the order of the Kolmogorov length scales, typically tens of microns in such flows. Such resolution is even necessary for laminar flows in regions, where the flow locally exhibits sharp velocity gradients in geometries like bends, bifurcations, junctions and separation zones.

---

<sup>1</sup> Corresponding author: Email address: Qianhui.Li@city.ac.uk

51 In general, in-vivo flow mapping using four-dimensional flow Magnetic Resonance Imaging (4D MRI) can achieve  
52 a typical spatial resolution of 1.5-2.5 mm, a temporal resolution of 30-60 ms and slice thickness of 5-8 mm (Stankovic  
53 et al., 2014). Higher resolution of the measured velocity profiles can only be achieved in relatively straight vessels  
54 (Katritsis et al., 2007). Another equally important factor is the accuracy in detecting the wall position relative to the  
55 velocity field, which remains a challenging task in 4D MRI (Zimmermann et al., 2018). There are only a few reports on  
56 the reproducibility and reliability of WSS estimation obtained from 4D MRI measurement (Markl et al., 2011). A  
57 combined study of 4D MRI measurement and CFD predictions on WSS in a laminar flow through a carotid bifurcation  
58 model has been reported in (Papathanasopoulou et al., 2003), concluding that the 4D MRI measurement was not able  
59 to detect the high WSS values along the inner walls of the bifurcation compared to the values predicted by the  
60 numerical simulation. As for the in-vitro measurement, V-PIV measurements suffer the same resolution problems. In  
61 addition, detecting the wall position is a non-trivial part. Kunze et al. (Kunze et al., 2008) first highlighted the  
62 importance of accurate wall-position information in 3D-PTV for accurate WSS measurements. To overcome the  
63 problem with the actual wall-position, they developed mirror-image 3D-PTV, where the original particle image and its  
64 mirror image reflected from the wall are used as additional inputs into the tracking data. Their results of a transitional  
65 wall-jet showed an excellent agreement between the calculated WSS and the theoretical values. In more complex  
66 geometries, 3D-PTV often requires utilization of larger particles of the order of 100  $\mu\text{m}$  in order to improve light-  
67 efficiency for sufficient exposure in the required high-speed recordings. In (Gülan and Holzner, 2018), particles with a  
68 diameter of 200  $\mu\text{m}$  have been used for 3D-PTV flow studies in the aortic arch. In contrast, a light-sheet-based PIV  
69 application can use micron-size tracer particles and therefore can achieve two orders of magnitude higher spatial  
70 resolution. This method has become a standard flow diagnostic technique for in-vitro studies (Raghav et al., 2018).  
71 However, it provides only the 2D in-plane velocity field and requires a much higher seeding density, which is  
72 sometimes difficult to achieve near the wall.

73 A novel tracer-less WSS measurement method with high potential for in-vitro applications in biological flows was  
74 introduced recently in (Bruecker et al., 2005); this is based on a high-resolution recording of the tip motion of wall-  
75 mounted flexible micro-pillar sensors, acting similar to micro-cantilever beams subjected to flow-induced drag forces.  
76 This method has recently been adapted to WSS measurements in aortic flows; results for different heart valve  
77 prostheses with 1 mm length micro-pillar sensors were reported in (Li et al., 2020), not without mentioning remaining  
78 limitations of these sensors regarding the spatial and temporal resolution and possible measurement uncertainties  
79 introduced by the sensor calibration procedure. To achieve an accurate measurement of the WSS with this technique,  
80 it is of great importance to calibrate the sensors in an appropriate way and under similar flow conditions as in the  
81 actual experiment (Bruecker et al., 2007). Ex-situ calibration might be not reliable for such applications as reported  
82 herein as it is hard to achieve the same working conditions in terms of flushness of wall-mounting of the elastic  
83 cantilevers, their clamping, the underlying flow conditions, possible changes of the elastomeric material parameters  
84 with time in the liquid or with temperature, to name only a few reasons.

85 In the present paper the sensors are calibrated in-situ with a single systolic flow pulse (the calibration pulse) and  
86 using reference data from complementary flow simulations at the same boundary conditions. For this procedure the  
87 aortic valve is exchanged with a thin tubular insert, which transforms the aorta phantom into a tubular bend with  
88 constant cross-section ( $180^\circ$  curved bend). For the phase of flow acceleration in the calibration pulse the flow remains  
89 laminar and homogeneous, which is used for calibrating the static and dynamic response of the sensors with input  
90 from the simulated velocity profiles in the boundary layer at the locations of the sensors. After the calibration, the  
91 tubular insert is exchanged with the actual mechanical heart valve (MHV) under investigation and the sensors are used  
92 to map the wall-shear (WS) evolution along the aortic wall distal to the valve under physiological flow conditions. It is  
93 the first time that such a CFD-assisted verification of the sensor response is possible at the same pulsatile flow  
94 conditions and geometrical conditions as in the actual experiment with MHVs. The present study goes further on  
95 addressing the issue of uncertainty in WSS measurements within such complex geometries as reviewed above. A  
96 recent study published during the review phase also hints on the lack of a systematic comparison between  
97 experimental and numerical values of the WSS for realistic aortic flow conditions (see (Corso et al., 2021)). The herein  
98 described methodology is new and completes the in-house built in-vitro flow tester with a reliable WSS measurement  
99 technique and provides a unique research facility for future hydrodynamic testing of heart valve prostheses with focus  
100 on WSS diagnostics. The methods are described in the following Section 2 and the results are given in Section 3, which  
101 is followed by discussions and conclusions.

## 102 2. Materials and Methods

## 2.1 Experimental study

### 2.1.1 Heart valve tester

Figure 1a shows a principle sketch of the aortic flow duplicator (heart valve tester) with the transparent model of the human aorta placed at the bottom of a liquid-filled transparent container (see also Figure 1b for the sketch of top view and Figure 1d for the actual frontal view of the experimental set up), with a smooth converging inlet nozzle with initial diameter  $D_N=40\text{mm}$  and length of  $2D_N$ . The flow through the model is generated with a programmable pulse generator as described in our previous study (Li et al., 2020). A 58%/42% by mass glycerine-water solution is used as working liquid having a density  $\rho_f = 1140 \text{ kg}\cdot\text{m}^{-3}$  and dynamic viscosity  $\mu = 5 \text{ mPa}\cdot\text{s}$  at  $38^\circ\text{C}$ . Therefore the fluid is considered as Newtonian, with constant kinematic viscosity of  $\nu = \mu/\rho = 4.386 \cdot 10^{-6} \text{ m}^2/\text{s}$ , and the aorta walls as rigid. Note that heart valve testers usually work with Newtonian liquids, first as the vessel diameter of the aorta is large and non-Newtonian effects can be neglected therein (see (Fung, 2013; Kim et al., 2004)) and secondly to ensure standardized working conditions between different testers when used for FDA regulation and approval. The air cushion above the liquid level is used to model systemic vascular compliance. The imposed flow profile is given in Figure 1c, which resembles a physiological systolic flow pulse with the maximum velocity reached at about 30% of the cycle, giving a peak Reynolds number of about 5400 (see section 2.1.2). The aorta phantom is fabricated from transparent Perspex and has the form of a regular 180-degree bend with a constant inner diameter ( $D_A=25 \text{ mm}$ ), curved along the plane of symmetry (see Figure 2).

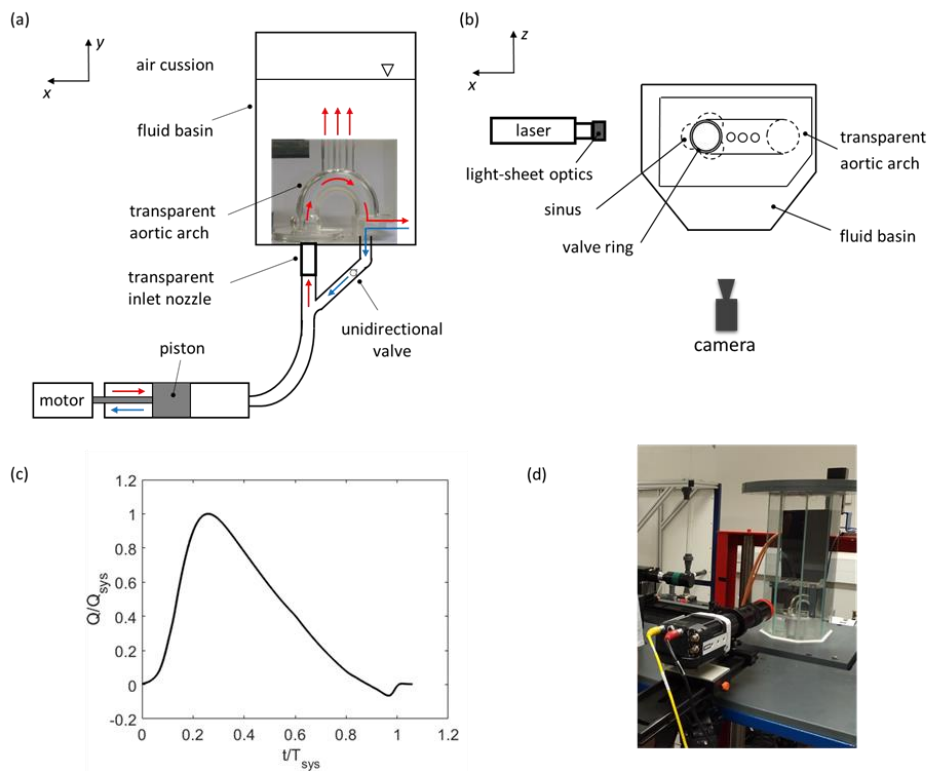


Figure 1. (a) Sketch of the pulse duplicator. (b) Top view of the experimental setup. (c) Inlet flow condition over the systolic cycle, where  $Q_{sys}$  is the peak flow rate and  $T_{sys}=386 \text{ ms}$  is the systolic time (d) Frontal view of the setup.

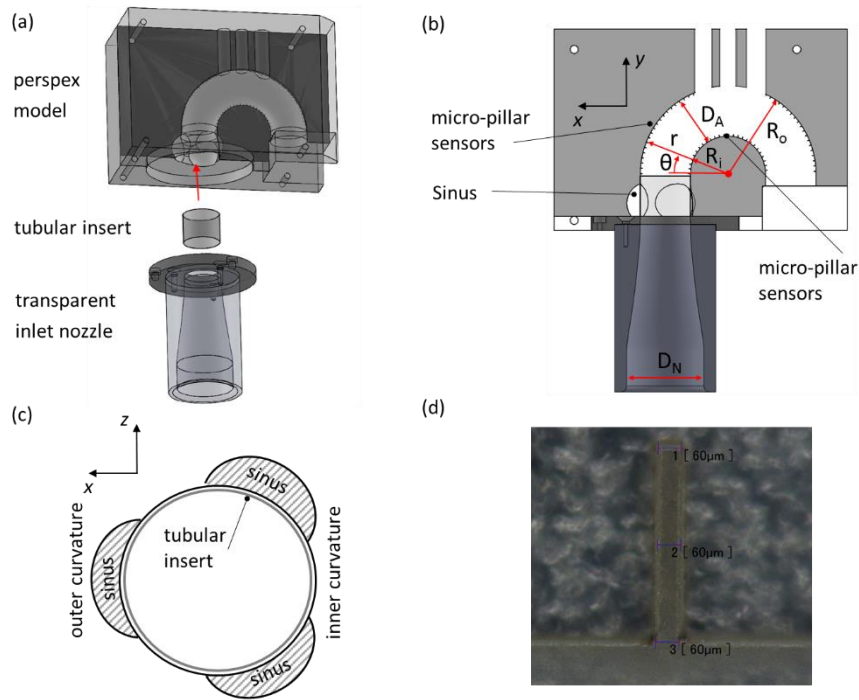


Figure 2. (a) Aorta model with removable tubular insert in the valve plane (b) Frontal view of the sensor placement in the symmetry plane of the aorta model (diameter of the inlet nozzle  $D_N=40\text{mm}$ , diameter of the aorta  $D_A=25\text{ mm}$ , radius of the inner curvature  $R_i=18\text{ mm}$ , radius of outer curvature  $R_o=43\text{ mm}$ ). (c) Cross-section in the valve plane. (d) Microscopic image of a single micro-pillar sensor.

Furthermore, there are three symmetric sinuses of Valsalva (SOV) at the aortic root and arterial branches at the top of the bend. The geometrical parameters of this model are the same as the silicone model used in (Li et al., 2020). The Perspex model is fabricated from two symmetric halves clamped together, sealed at the centre plane with a thin elastic silicone sheet (Wacker ELASTOSIL Film 2030 Wacker Chemie AG, Munich, Germany. Film thickness  $200\ \mu\text{m}$ , post-curing density:  $\rho_s=1500\ \text{kg}\cdot\text{m}^{-3}$ , Shore A: 27, elastic modulus  $E=1.34\ \text{MPa}$ ). The circular edge of the sheet is micro-structured such that it contains a row of radially outgoing extensions of rectangular flexible cantilever beams, i.e. the micro-pillar sensors. The dimensions of the micro-pillar are as follows: beam length  $L=500\ \mu\text{m}$ , beam thickness  $h=60\ \mu\text{m}$ , beam width  $b=200\ \mu\text{m}$ . The microscopic structure of the micro-pillar shown in Figure 2d was measured by a digital microscope (VHX-700F, KEYENCE Ltd, UK) equipped with a VH-Z20R lens. The inner part of the edge follows the extrados of the aorta and is flush to the wall such that the root of the sensors is clamped between both halves of the model. The angular location of these micro-pillars starts from  $\theta=0^\circ$  with an angular interval of  $7^\circ$  at the inner wall and  $3.5^\circ$  at the outer wall.

In the calibration procedure, a thin-walled tubular insert (outer and inner diameters of 25 and 24.6 mm, respectively) is placed in the arch at the same location where typically the aortic valve is located. When the systolic flow pulse is generated, the bulk flow smoothly enters through the step-free inlet into the tubular bend. WS measurements in this flow pulse are compared to the reference data of the CFD simulations (see section 2.2 and Appendix B) to verify the calibration. Thereafter, the tubular insert is removed and the actual MHV prosthesis is inserted at the entrance of the aorta. The same systolic flow pulse is then applied again to investigate the WS at the aortic walls distal of the valves. The different types of MHVs are the same as used in (Li et al., 2020) and are displayed in Figure 3 in open and closed situation, including the St. Jude Medical Regent bileaflet mechanical heart valve (SJM Regent valve) (St. Jude Medical Inc., Minnesota, U.S.) and the Lapeyre-Triflo FURTIVA trileflet mechanical heart valve (Triflo valve) (Novostia SA, Neuchâtel, Switzerland).

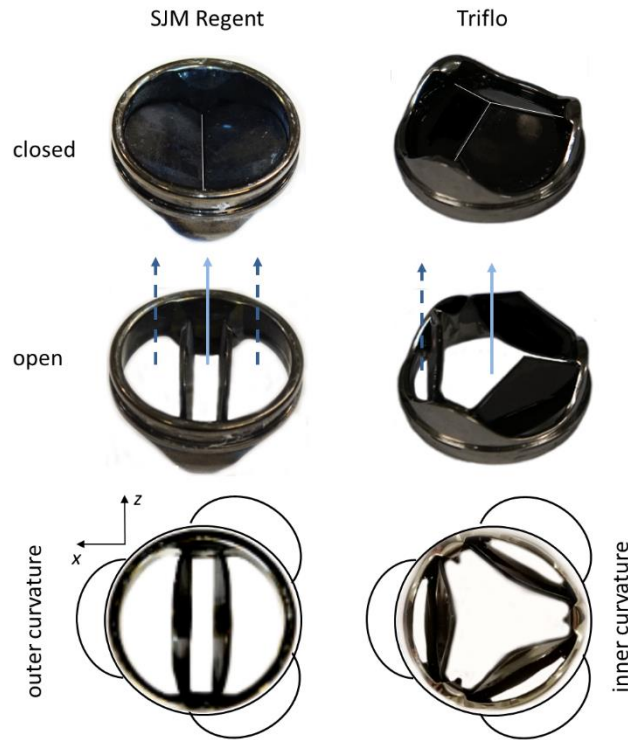


Figure 3. SJM Regent valve: one leaflet is facing the left sinus at the outer curvature of the aorta while the other leaflet is in the middle between two sinuses, facing the inner curvature. Triflo valve: the axes of the leaflets face the sinuses in all three directions.

### 2.1.2 Flow measurements using High-Speed Particle Image Velocimetry (HS-PIV)

Complementary flow field measurements have been also obtained using High-Speed Particle Image Velocimetry (HS-PIV) in the silicone model, as presented in (Li et al., 2020) ; as already mentioned, this has the same geometry as the Perspex model but offers better optical quality in regions deep inside the arch. The arrangement of the experimental setup is shown in Figure 1b. A continuous wave Argon-Ion laser (Raypower 5000, 5W power at  $\lambda=532$  nm, Dantec Dynamics) is used as an illumination source. The output laser beam is approximately 1.5mm in diameter and is further expanded into a sheet, illuminating the symmetry plane of the aorta. Small tracer particles (fluospheres, Dantec Dynamics, mean diameter 30  $\mu\text{m}$ , and density  $\rho_p = 1040 \text{ kg} \cdot \text{m}^{-3}$ ) are added to the working liquid. For all recordings, a high-speed camera (Phantom Miro 310, Ametek) equipped with a lens (Tokima Macro f=100 mm, F 2.8) is used.

PIV measurements with three different fields of view are performed, including a full field PIV measurement for the global flow field of the ascending aorta (AAo), zoom-in PIV measurement covering the diameter of the aorta ( $D_A$  corresponds to a scale of 688 pixels on the image sensor) to measure the axial velocity profile along cross-section e.g.  $\theta=21^\circ$ , as well as micro-PIV measurement for capturing the near wall flow field. The measurement configurations are listed in Table 1. An in-house developed MATLAB code is used to post-process the flow field recordings, which contains the image pre-processing and 2D cross-correlation of successive images to calculate the particle displacements with subpixel accuracy using a Gaussian fit of the correlation peak in the correlation plane, a standard method in Digital Particle Image Velocimetry (DPIV) (see (Raffel et al., 2018a)). The data processing process has also been described by the authors' in (Li and Bruecker, 2018). Processing is done in small interrogation windows with an iterative grid refinement method. The configurations of the final window size and the overlap ratio are also given in Table 1.

Table 1. Configurations of optical measurements and data processing.

Region of interest	Frame rate (fps)	Resolution (px <sup>2</sup> )	Field of view (mm <sup>2</sup> )	Interrogation window (px <sup>2</sup> )	Overlap ratio (%)
Full-field PIV	5400	576 × 768	57.6 × 76.8	32 × 32	50
Zoom-in PIV	5400	576 × 768	20.9 × 27.9	128 × 16	50
Micro-PIV	7200	576 × 768	7.6 × 10.2	190 × 48	75
Micro-pillar	2000	1280 × 800	8.5 × 5.3	32 × 24	75

The peak inlet velocity observed in the plane of the circular entrance into the bend reaches a value of  $U_p = 0.95$  m·s<sup>-1</sup>. The Reynolds number, defined with the peak velocity, is  $Re = \frac{\rho U_p D_A}{\mu} = 5415$ . This indicates a turbulent flow in the peak flow situation. However, in pulsatile flows, the transition to turbulence also depends on the Womersley number ( $\alpha$ ) and the pulsation amplitude (A) (Stettler and Hussain, 1986; Trip et al., 2012). These parameter in the present study are  $\alpha = \frac{D_A}{2} \sqrt{\frac{\omega \rho}{\mu}} = 16$  and  $A = U_p / U_m = 5$ , where  $\omega$  is the driving frequency. A variety of studies (Stettler and Hussain, 1986; Xu et al., 2017) on pulsating pipe flows for Womersley numbers  $\alpha > 10$  have reported that the transition in such cases is further delayed into the deceleration phase. This agrees with our observations as shown by the flow visualization picture in Figure 9 taken at the peak systole time, which demonstrates a laminar and homogeneous flow in this flow channel. In the following, laminar flow is used for the calibration of the WSS sensors.

### 2.1.3 Micro-pillar sensor methodology

Micro-pillar WSS measurements follow the principle of measuring the bending of a one-sided clamped microscopic cantilever beam, situated in the boundary layer and actuated by the drag forces from the flow around the pillar; the measurement principle and methodology is given in detail in (Bruecker et al., 2007; Bruecker et al., 2005). Theoretically, when the length of the pillar is small enough such that it is fully submerged in the viscous sublayer of the near-wall flow boundary layer, the flow-induced bending moment  $M$  is proportional to the WSS, which can be measured by the tip displacement of the micro-pillar relative to its position at fluid rest. As shown in our previous work (Bruecker et al., 2007; Bruecker et al., 2005), the dynamic response of such a micro-pillar sensor in liquids follows closely that of a 2<sup>nd</sup> order harmonic oscillator in overdamped situation (quality factor  $Q < 1/\sqrt{2}$ ), which is described by a nearly constant gain until the cut-off frequency  $f_c$ , where the gain rolls off. The amplitude and phase response of such an oscillator are given by (Van Eysden and Sader, 2006):

$$|H(j\omega)| = \frac{1}{\sqrt{\left(1 - \frac{\omega^2}{\omega_n^2}\right)^2 + \frac{1}{Q^2} \frac{\omega^2}{\omega_n^2}}}, \quad \varphi(j\omega) = -\arctan\left(\frac{1}{Q} \frac{\omega \cdot \omega_n}{\omega_n^2 - \omega^2}\right) \quad (1)$$

with the flexural natural frequency  $\omega_n$  in the liquid environment. For a rectangular cantilever beam  $\omega_n$  is related to the natural frequency  $\omega_{n,vac}$  in vacuum as follows (see (Van Eysden and Sader, 2006)) :

$$\omega_n = \omega_{n,vac} \left(1 + \frac{\pi \rho_f b}{4 \rho_s h}\right)^{-1/2}, \quad \omega_{n,vac} = \frac{1.875^2}{L^2} \sqrt{\frac{EI}{bh\rho_s}}, \quad (2)$$

where  $E$  is the Young's modulus and  $I$  the moment of inertia of the beam cross-section, which is  $I = bh^3 / 12$  for a rectangular beam. With the given data, the expected resonance frequency (flexural) for the sensor in the liquid used herein is estimated to be  $\omega_n = 4210$  rad/s, which takes into account the added mass effect of the viscous liquid surrounding the sensor. From that we can estimate the measurement range, defined as the range of nearly constant gain (and small phase shift) below the cut-off frequency  $f_c = 0.3 \omega_n$ . This theoretical estimation will be verified later by experimentally determined values of the gain, cut-off frequency and quality factor  $Q$  from the herein described CFD-assisted calibration of the sensor response.

Of further importance to characterize the sensor properties is the sensitivity  $S$ . According to (Bruecker et al., 2005), the sensitivity could be defined as the ratio of the pillar tip deflection amplitude  $Q_s$  to the wall shear stress. As the pillar tip's deflection is proportional to the flow-induced bending moment  $M$ , we use herein the definition of the sensitivity as  $S = M/\gamma$ , where  $\gamma$  is the wall shear rate. Theoretically, for very small pillars, the sensitivity should remain constant which is then determined ideally within a defined shear flow, e.g. a specially adapted cone-plate type viscometer as shown in (Bruecker et al., 2005). However, the flow condition we are investigating herein is a pulsating flow with a developing boundary layer with time-varying velocity profiles. Therefore, further analysis is required to understand the effect of velocity profile shape, boundary layer thickness and velocity magnitude on the sensitivity. This is done herein for the micro-cantilever beams in analogy to the derivations made for slender wind-hairs in the work from Dickinson (Dickinson, 2010). The pillar is considered as a one-sided clamped cantilever beam (linear-elastic Euler-Bernoulli beam theory) with maximum deflection less than 10% of the pillar length. Furthermore, the bending moment acting on the beam is determined from the quasi-steady flow approximation of the local drag. The calculation of the resultant moment at the base of the pillar is as follows (Dickinson, 2010)

$$M(t) = \int_0^L g(t, \xi) \xi d\xi, \quad (3)$$

where  $g(t, \xi)$  is the instantaneous load intensity that acts normal to the longitudinal axis with units of force per unit length at any longitudinal location  $\xi$ .  $g(t, \xi)$  could be estimated as

$$g(t, \xi) = \frac{1}{2} C_d (Re_\xi) \rho_f b u(t, \xi)^2, \quad (4)$$

where  $\rho_f$  is the fluid density,  $b$  is the width of the beam,  $u$  is the flow velocity incident on the longitudinal axis of the pillar and  $C_d$  is the drag coefficient.  $C_d$  is determined as a function of the local Reynolds number. It has been reported that at low  $Re$  ( $Re < 10^2$ ) different shape of the cross section shows a similar relationship of drag coefficient with the  $Re$  (Prandtl, 1952; Yuce and Kareem, 2016). We herein use the same relationship as introduced by Dickinson (Dickinson et al., 2012; Dickinson, 2010) which uses a least-squares fit to empirical data ((Prandtl, 1952), p.190) for the drag coefficients of long circular cylinders in cross-flow at  $Re_\xi = 10^{-1}, 10^{-0}$  and  $10^1$  with the R-squared value of 0.996, leading to the following linear logarithmic expression:

$$\log C_d = -\frac{2}{3} \log Re_\xi + \frac{5}{2}, \quad (5)$$

where  $Re_\xi = \frac{u(t, \xi) b}{\nu}$ . According to (Dickinson et al., 2012), Eq. (5) assumes an infinite cylinder in cross-flow and the end effect of the finite length of pillar is not accounted. Previous study by Jana et al. (Jana et al., 2007) has shown that  $C_d$  varies by less than 5% for cantilevers with 10:1 and 200:1 aspect ratio in steady flow when  $1 < Re_\xi < 63$  which covers the  $Re_\xi$  of the present study, indicating that end effects are small.

Substituting the load intensity Eq. (4) into the resultant moment Eq. (3), it yields

$$M(t) = \int_0^L \frac{1}{2} C_d (Re_\xi) \rho_f b u(t, \xi)^2 \xi d\xi \quad (6)$$

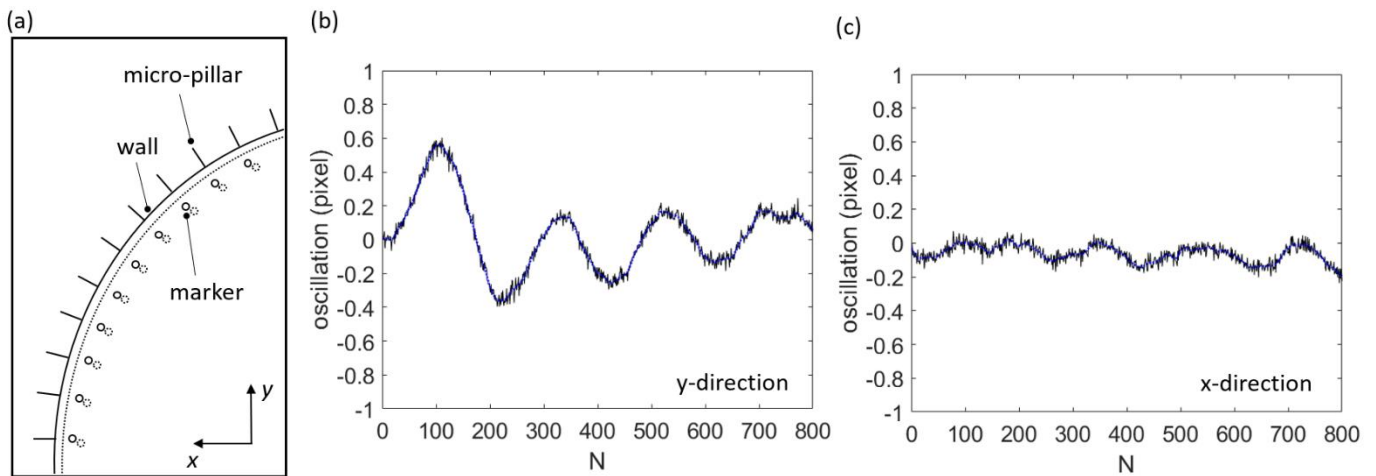
Later in section 3.2 in the paper we use Eq. (5) and (6) to determine the sensitivity of the sensor with data from the local velocity profiles around the sensors, which are obtained from the CFD.

#### 2.1.4 Digital image processing of the sensor tip displacement

The tip bending of the sensors at the symmetry plane of the Perspex model of the aortic arch is recorded with a digital camera for all sensors simultaneously and transferred via image processing into a tip displacement vector, which is tangential to the wall. The high-speed camera used is the Phantom Miro 310 Ametek, equipped with an inverted telescopic lens (Model K2/SC™, Infinity Photo-Optical Company, Boulder, CO); a resolution of 1280×800 pixels, recording at 2000 fps was utilized. These settings are listed also in Table 1. It provides a field of view of 8.5×5.3 mm<sup>2</sup> as shown in Figure 5a, and captures the motion of an array of 11 micro-pillars located at the inner curvature simultaneously with a resolution of 150 pixels/mm. To improve the contrast in the images, the tips of the sensors are fluorescent-labelled by fluorescent micro-spheres (PMMA-RhB-Frak-Particles, Dantec Dynamics, peak emission at 584 nm, peak absorption at 540 nm), which have maximum absorption near the wavelength of the illuminating laser light. A long pass filter (transmission wavelength: 560 - 1650 nm, Edmund Optics Ltd) was applied to block all light from the laser and reflections from the aorta model, and thus, only transmitting the light of the fluorescent-labelled tips. Thus, the tips of the micro-pillar appear as bright dots against a black background. Additional fluorescent markers at the inner wall of one half of the aorta model provide data on a possible motion of the model during the flow pulse. The processing steps of the measurement chain are listed as follows: a) detect vibrational model motion by marker processing, b) subtract vibrational model motion by image transformation, c) dewarp images such that the circular

286  
287  
288  
289

arcs along the polars of constant pillar height unfolds into a linear unwrapped image segment, d) process the tip displacement between the unfolded images at rest and in the flow pulse, e) postprocess the data. In this section the data are presented in pixels units to present the tip displacement values in relation to the pixel resolution of the camera (for conversion to physical displacement in mm use the optical conversion factor 1 mm= 150 px).

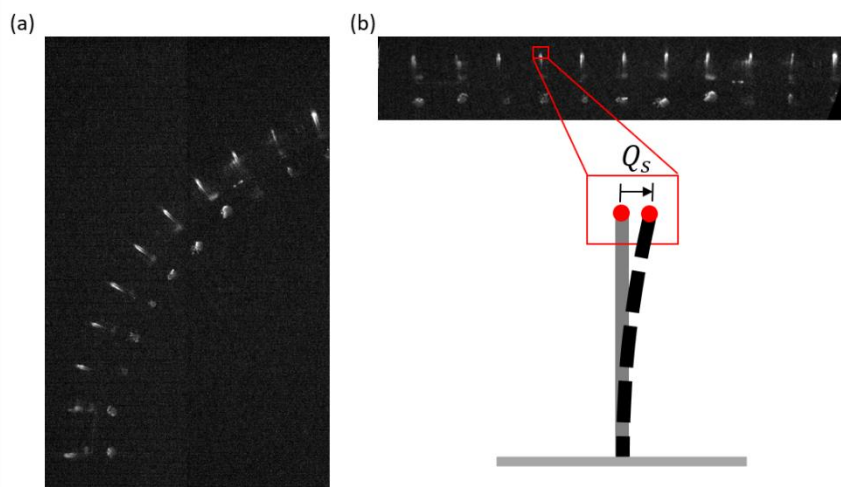


290  
291  
292  
293  
294  
295  
296

Figure 4. Correcting for vibrational motion of the whole aorta model. (a) capturing the vibrations in the images during the flow pulse ( $N$  = index of the image number in the sequence) by processing the marker positions and comparing those to the position at rest via 2D cross-correlation. Illustration of shift of the model seen by the dislocated positions (dashed marker) relative to the marker to the situation at fluid rest (solid markers). (b) and (c) typical profiles of vertical and horizontal motion of the model during the flow pulse.

297  
298  
299  
300  
301  
302  
303  
304  
305  
306  
307  
308

Figure 4 shows a typical vibrational motion of the model during the flow pulse, which was obtained by tracking markers on the inner side of the model using a 2D cross-correlation procedure similar as in DPIV (Raffel et al., 2018a). In the next step, those data are used to preprocess the image sequence such that the vibrational motion of the aorta model in the flow pulse is corrected to zero in the complete image sequence from begin to the end of the flow pulse (the marker position then exactly overlap in the whole sequence). This is done via a 2D linear image translation (bilinear interpolation) to correct the relative motion. In the next step, another image interpolation is done to unfold the polar arrangement of the pillars presented in Figure 5a such that they appear relocated along a straight line with the tangential displacement of the pillar's tip now converted to the horizontal direction as shown in Figure 5b. Finally a 2D cross-correlation processing similar as in DPIV (see (Raffel et al., 2018a)) is used to detect the pillar tip motion (comparing flow-off with flow-on situation) in small interrogation windows located at the centre of the pillar tips of  $32 \times 24 \text{ px}^2$ ; see the zoom-in view of the interrogation window in Figure 5b. Again, subpixel resolution is achieved by fitting the correlation peak similar as in DPIV.



309  
310  
311

Figure 5. (a) Original image showing the polar arrangement of the micro-pillar WSS sensors at the inner curvature of the aortic arch and (b) after unfolding the polar coordinates into a horizontal coordinate by dewarping the image (a).

A subset of enlarged windows shows the typical windows of the pillar tip (at the situation of no-flow and flow with a displacement of pillar's tip  $Q_s$ , which are used for the 2D cross-correlation procedure (note that the relative shift is only about 2 px in the images).

The tip displacement from the measurements can be resolved down to a resolution of  $0.4 \mu\text{m}$  (minimum resolution in pixel =  $0.06 \text{ px}$ ). This limiting value calculates from the error-propagation of the standard error of all digital image processing steps including vibrational motion correction, image dewarping and tip displacement detection using 2D cross-correlation. The combined standard error is calculated as  $\sigma_c = 0.06 \text{ px}$ , which corresponds to a physical scale of  $0.4 \mu\text{m}$ , hence defining the resolution limit. Note, that a camera with higher pixel resolution than the one used herein can provide higher accuracy, proportional to the increase in pixel resolution.

### 2.1.5 Data post-processing

The signal processing chain of the tip displacement data is illustrated in Figure 6 exemplary for the tip displacement of the pillar at  $\theta = 21^\circ$  over the full number of images in the recorded sequence of the calibration pulse ( $N = \text{index of number of image in the sequence}$ , conversion in time is by  $N_{\text{systole}}/T_{\text{sys}} = 772/386 \text{ ms}$  where  $N_{\text{systole}}$  is the total image number of the systolic cycle). Again, the data are presented in pixels units over image number to present the raw data in relation to the pixel resolution and high-speed frame-rate of the camera. The profile indicates a maximum value of the tip displacement of about 2 px, corresponding to  $13.3 \mu\text{m}$  (minimum resolution  $0.4 \mu\text{m}$ ) which is 2.66% of the length of the micro-pillar. Because of such small bending the pillar tips remain nearly at the same wall-normal distance in the images (Bruecker et al., 2007). A Fourier series curve fitting procedure (The MathWorks) has been applied (series of 7 sine curves) to remove high-frequency oscillations from the data. Because of the open endings of the model, the flow experiences an impedance jump which causes part of the flow pulse to be reflected back (known as artificial dicrotic notch in pulse-duplicators, see (Politi et al., 2016)). This reflection overlaps with the original flow pulse signal and causes a small oscillation in the sensor signal during flow deceleration at the late phase of the systolic pulse. The outlet boundary conditions within the CFD simulations prevent such a reflection, hence for a direct comparison of the experiments with the CFD data it is required to remove this artificial oscillation from the signal. Test with different band-pass filter finally showed, that the overlaying oscillation due to the dicrotic notch can be approximated mathematically with the profile of a sine-Gaussian pulse:

$$f(N) = A \cdot \sin\left(\frac{2\pi N}{\lambda} + \varphi\right) \cdot e^{-\frac{1}{2}\left(\frac{N-\mu}{\sigma}\right)^2}. \quad (7)$$

The coefficients best fitting the artificial dicrotic notch were determined as follows: magnitude  $A = 0.23 \text{ px}$ , wavelength  $\lambda = 160 \text{ images}$  (corresponding frequency  $12.5 \text{ Hz}$ ), phase shift  $\varphi = \frac{2\pi}{\lambda} \cdot 411 \text{ images}$ , center position of the pulse at image number  $N = 381$  and standard deviation  $\sigma = 100 \text{ images}$ . This form of the reflection pulse is seen on all sensors at the same time and was removed from the original signal by subtracting Eq. (7) before the curve fitting is applied (Fourier series, 7 sine curves). This is the final data set of the pillar tip bending, which has removed all fluctuations above frequencies of  $150 \text{ Hz}$ , which are considered as non-coherent and random in the range of investigated flow conditions.

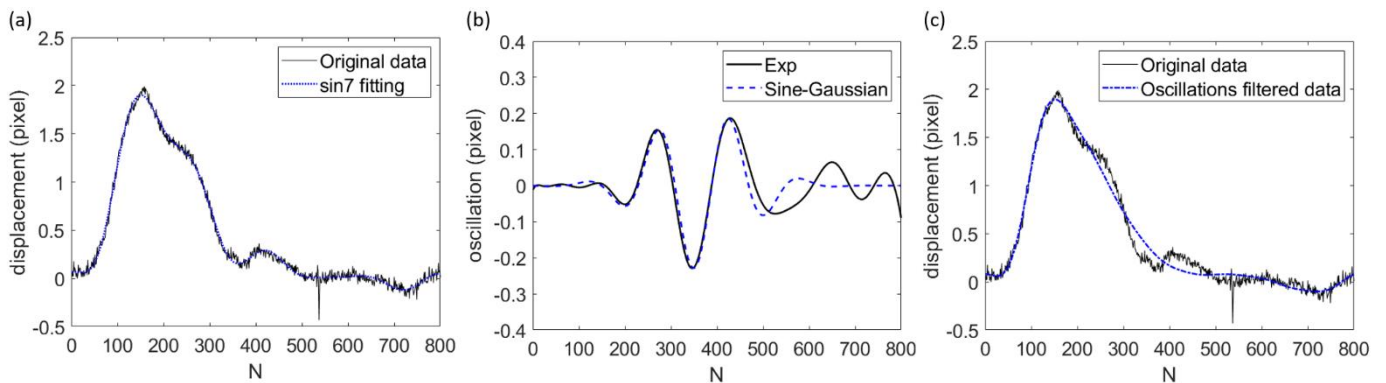
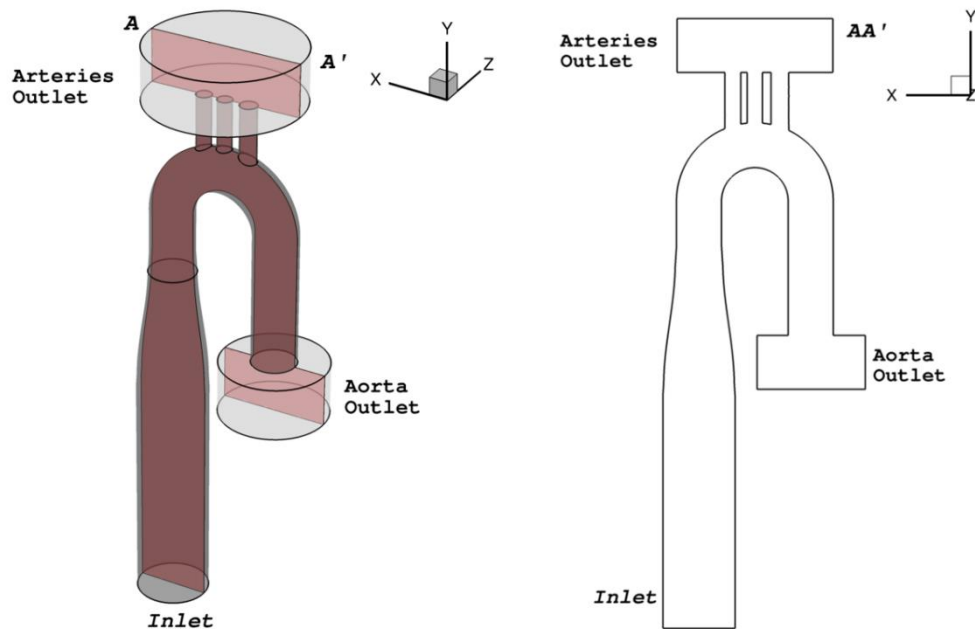


Figure 6. (a) Plot of the measured sensor signal in the calibration pulse, shown by the black line and overlaid with a Fourier series fitting denoted by the blue dot line. (b) Small-amplitude oscillation of the tip displacement induced by the pressure pulse reflection at the open endings of the aorta model (artificial dicrotic notch) and fit with a Gaussian-modulated sinusoidal curve. (c) Tip displacement after removal of the artificial dicrotic notch effect.

353

354 **2.2 Numerical simulations**355 **2.2.1 Set up of the computational domain**

356 Numerical simulations of the flow are performed using OpenFOAM (Weller et al., 1998). The flow simulations are  
 357 carried out on an aorta model, identical to the geometry used in the calibration experiments, with the tubular insert  
 358 covering the sinus region. Identical to the experiments, the fluid is considered as Newtonian, with constant kinematic  
 359 viscosity of  $\nu = \mu/\rho = 4.386 \cdot 10^{-6} \text{ m}^2/\text{s}$ , and the aorta walls as rigid. The reason for that simplification is the  
 360 purpose of the CFD study to support the calibration of the sensors used in the heart valve tester (see Appendix B for  
 361 a detailed discussion of the rheology of blood). Cylindrical flow compartments are added at the outlets of the aorta  
 362 and the arterial branches to facilitate open-end boundary condition as in the experiments, as shown in Figure 7. At the  
 363 inlet, the time dependent volumetric flow rate, measured during experiments, is assigned as boundary condition and  
 364 a uniform block velocity profile along the diameter is imposed. The upstream extension of the inlet nozzle is chosen  
 365  $4D_N$  long so that the flow would be developed before the converging part; the length of the extension is determined  
 366 by numerical tests of the same pulsatile flow on a long straight tube. On the outlet volumes, zero-gradient velocity  
 367 and fixed total pressure boundary conditions have been assigned, replicating the experimental conditions. The total  
 368 pressure is set equal to ambient atmospheric pressure (1bar) and thus the static pressure to be imposed is calculated  
 369 using the local velocity value. Standard no-slip velocity boundary conditions are imposed on the aorta walls.  
 370



371

372 Figure 7. The computational domain of the aorta model. The inlet has a total length of  $6D_N$  ( $4D_N$  before the convergent  
 373 part). Two volumes have been put at the outlet of the aorta and the outlet of the arterial branches. The plane AA'  
 374 corresponds to the side centre plane. The nozzle has a diameter of  $D_N=40\text{mm}$ .  
 375

376

377 For pulsatile vascular flows different meshing approaches can be used, as described in (Tu et al., 2015). In the  
 378 current numerical study, because the domain consists of the aorta, as well as three arterial branches, an unstructured  
 379 tetrahedral mesh is used. The choice of the tetrahedral mesh is based on its automatic, fast and straightforward  
 380 generation process.

381

382 The walls and the boundaries of the computational domain are triangulated, then structured layers are inserted  
 383 over the walls to better resolve the boundary layer and finally the volume is discretised by unstructured tetrahedral  
 384 cells. The aortic arch is discretised by 248 cells on the circumference and 130 along the inner and 300 outer arch,  
 385 resulting in a triangular mesh of characteristic size between  $D_A/80$  and  $D_A/57$ . In addition, 10 cell layers over the walls  
 are added, with growth ratio 1.2 and first cell size  $y_1 = 0.0396 \text{ mm}$ , which adheres to the condition of  $y_+ \leq 1$  that,  
 considering the peak velocity Reynolds number, sets as a limit the value  $y_1^* = 0.0594 \text{ mm}$ . The sum of the 10 layers

covers the total height of an estimated boundary layer thickness of 1mm, the first cell's height corresponds to the 0.4% of the boundary layer and the last cell's height to the 20.5%. The layers are constructed by inflation of the boundary triangular cells, thus forming structured prism cells next the wall. The core volume of the mesh is composed by homogeneous tetrahedra with characteristic size  $D_A/100$  in the aortic arch. The grid coarsens towards the inlet and outlets. This results in a 9 million cell mesh. A thorough description of the computational mesh along with a grid independence study and a discussion about the spatial resolution are presented in Appendix B. Three meshes have been tested and the one described hereabove is the medium mesh, referred as middle; results presented hereafter refer to this middle mesh.

### 2.2.2 The computational algorithm

The PIMPLE algorithm (Moukalled et al., 2016) was used to solve numerically the incompressible Navier-Stokes equations

$$\nabla \vec{u} = 0, \quad (8a)$$

$$\frac{\partial \vec{u}}{\partial t} + \nabla \vec{u} \vec{u} = -\nabla \frac{p}{\rho} + \nabla v(\nabla \vec{u} + (\nabla \vec{u})^T), \quad (8b)$$

In the simulations performed, the stress term (second on the right-hand side of Eq. (8b)) is calculated and not modelled. The transient nature of the pulsatile flow under consideration characterized by a high Womersley number, along with the moderate Reynolds number of the flow, suggests that turbulence is not developing throughout the first part of the systolic cycle until peak flow. Rather, turbulence is expected to play an increasingly important role during the deceleration phase (after peak systole) where flow separation develops and transition initiates, see also (Stettler and Hussain, 1986; Trip et al., 2012) (See Appendix B for more details).

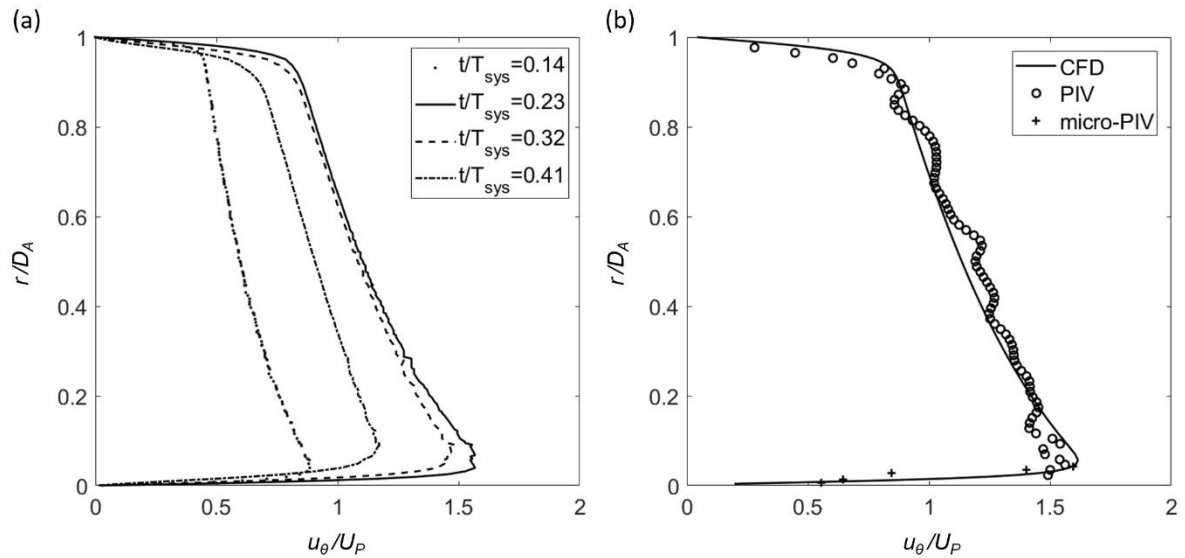
An implicit Crank-Nicolson scheme is chosen for the time integration and a second-order central differencing scheme is used for the spatial discretisation. The time step is automatically adjusted in order for the maximum calculated Courant number to always respect Courant-Friedrichs-Lewy (CFL) condition  $Co_{max} = \Delta t \frac{1}{2V} \sum_{faces} |\phi_i| \leq 1$ , with regards to the magnitude of the fluxes  $\phi_i$  on the faces of the computational cells. Additionally, the maximum time-step is restricted to 0.1 ms, in order to ensure that all the structures of the flow are resolved.

## 3. Results

From the simulations, velocity data are extracted along the diameter of the aorta on the locations of the micro-pillars and the WS is calculated. Except otherwise stated, the numerical results reported in the following paragraphs correspond to the side view central plane  $AA'$ , annotated in Figure 7, where also the array of micro-pillars is placed. The micro-pillar located at  $\theta=21^\circ$  cross-section has been selected to present the experimental results, to compare with the numerical predictions and to be used for the calibration of the measurement apparatus.

### 3.1 Global flow field and boundary-layer

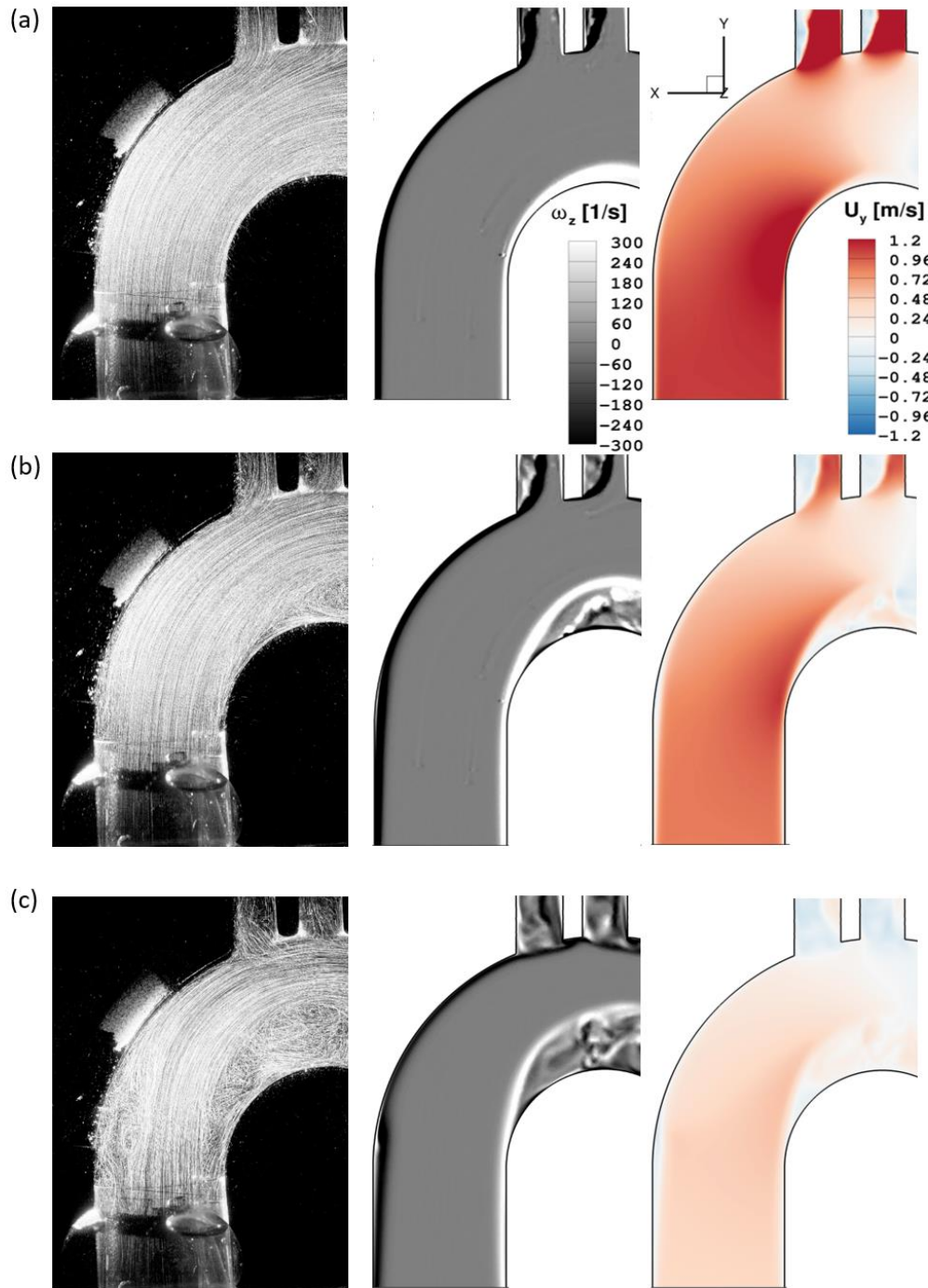
In Figure 8(a), the axial velocity profile as calculated by the CFD simulation is plotted, on four different instances along the pulse. The development of the boundary layer over the walls of the aorta and the absence of recirculation in the specific position, are clearly shown. The boundary layer is continuously growing in the flow pulse from zero at rest to about 1 mm at the early ramp ( $t/T_{sys} = 0.14$ ) and finally to a thickness of about 1.5 mm at the peak ( $t/T_{sys} = 0.23$ ), which shows the dynamic evolution of the boundary layer in the cycle. See Appendix A for further details.



424 Figure 8. (a) Axial velocity profile evolution along the pulse, at the cross-section  $\theta=21^\circ$ , on the centre plane AA', as  
 425 predicted from CFD simulations. The vertical coordinate corresponds to the radial position along the cross-section of  
 426 the aorta, measured from the inner wall towards the outer wall. (b) Comparison of experiment and CFD at one instant  
 427 ( $t/T_{sys} = 0.23$ ): Zoom-in PIV measurement of the core flow (open circular symbols), micro-PIV measurement at the  
 428 near-wall region (plus-symbols).  
 429  
 430

431 The comparison of the instantaneous experimental data and the numerical velocity profiles presented in Figure  
 432 8b shows a good agreement in the core flow region. The experiments show some small-amplitude modulations, which  
 433 are identified as peak-locking (Raffel et al., 2018a). Close to the walls, the results from the zoom-in PIV measurements  
 434 show lack in spatial resolution, while the micro-PIV results are able to resolve the stronger gradients.

435 Figure 9 presents the evolution of the flow field in the ascending part of the aorta, as seen in the experiments  
 436 and as predicted by the simulations. Experimental pathlines plotted as the trajectory of the tracer particles are  
 437 compared with in-plane velocity and out-of-plane component of vorticity contours on the centre plane AA' of the CFD  
 438 results. In the acceleration phase, the flow is homogeneous and remains fully attached to the walls of the ascending  
 439 aorta. Later in the cycle, flow separation initiates on the inner wall at a location downstream of the apex ( $\theta=90^\circ$ ), which  
 440 then develops and extends further while the separation point moves upstream. Still, the bulk of the flow remains  
 441 laminar and attached to the outer wall until  $0.63T_{sys}$ , when a slender separation region can be observed near the  
 442 entrance of the bend. Overall, for half of the systolic cycle until about  $0.5T_{sys}$  the flow structure between experiment  
 443 and CFD results show good agreement; it should be stressed that only the ramp-up part of the flow pulse ( $0 < t < 0.2$   
 444  $T_{sys}$ ) is relevant for the calibration. Therefore it should also not be surprising to notice differences to the experiments  
 445 in the late phase of the flow pulse with separating shear layers, secondary vortices and stagnant zones, which is  
 446 difficult to recapture with the laminar flow simulation.



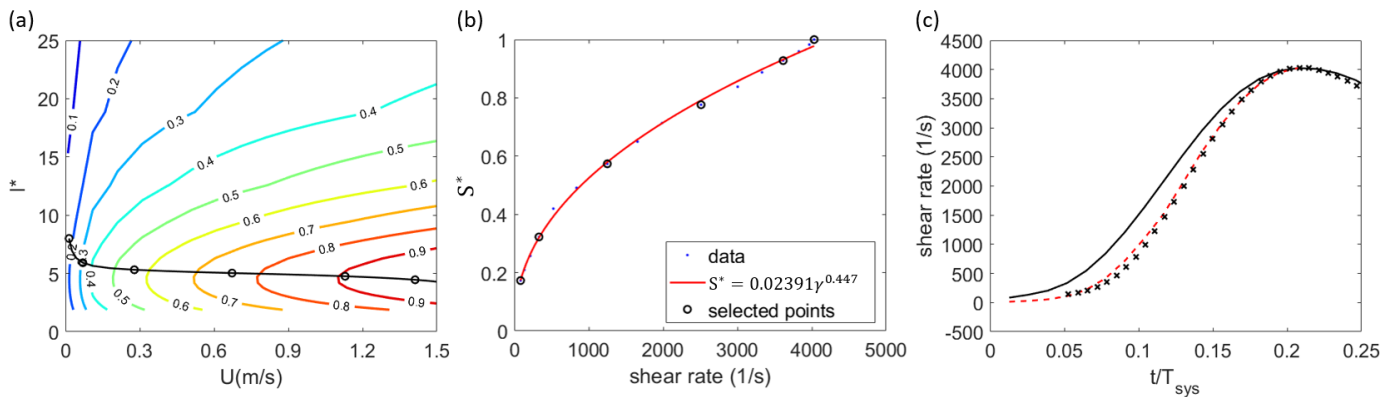
447

448 Figure 9. Flow pathlines (left column) extracted from the HS-PIV experiments, vorticity contours (middle column) and  
 449 velocity contours (right column) along the centre plane AA', as derived from the CFD simulations, at (a)  $0.23T_{sys}$ , (b)  
 450  $0.41T_{sys}$  and (c)  $0.63T_{sys}$ .  
 451

452 **3.2 Parameter sensitivity analysis**

453 To identify the parameters influencing the sensor sensitivity, we use the analytical methods described in section  
 454 2.1.3 in analogy to the derivations made for slender wind-hairs in the work from Dickinson (Dickinson, 2010). This is  
 455 to understand the effect of velocity profile shape, boundary layer thickness and velocity magnitude on the sensitivity.  
 456 The near-wall velocity profiles obtained from CFD are used as inputs into Eq. (5) and (6) for different times in the  
 457 calibration pulse and the sensitivity  $S$  is calculated. The geometrical and material parameter are taken from the given  
 458 sensor and the moment is calculated with the selected fluid parameter in the experiment. Iso-contours of the

459 sensitivity for the sensor at position  $\theta=21^\circ$  are given in Figure 10a as a function of the relative pillar length  $l^* = L/\delta_2$   
 460 (ratio of pillar length to the boundary layer momentum thickness) and the characteristic free-stream velocity  $U$  (the  
 461 velocity at the edge of the boundary layer). For relative low velocities in the early phase of the flow pulse, the dominant  
 462 parameter for the sensitivity is the magnitude of the velocity itself (the sensitivity is low for the whole range of  
 463 simulated pillar length). With increasing bulk flow velocity, the parameter of the boundary layer thickness gets of  
 464 larger influence. The sensitivity is low when the relative pillar length is large (length  $l^*>15$ , i.e. the boundary layer  
 465 thickness is thin with sharp velocity rise) or when it is very small (length  $l^*<2$ , i.e. the boundary layer thickness is very  
 466 large with weak velocity rise). Thus the highest sensitivity appears in a certain range of the relative length values. For  
 467 the flow condition investigated herein which is plotted in Figure 10a by the black line, we see that there is only slight  
 468 change of the relative pillar length values from  $l^* = 8$  at the very beginning of the acceleration phase ( $\sim 0.01T_{sys}$ ) to  
 469  $l^* = 4.3$  at the peak systole ( $\sim 0.23T_{sys}$ ) for a large range of the characteristic velocity ( $0 < U < 1.5$  m/s). Furthermore,  
 470 the sensitivity reaches a plateau-like region when the characteristic velocity is above 1 m/s and for the full range of  
 471 values of  $l^*$  covered herein. In this region the sensitivity remains within 90% of the maximum between the contours  
 472 of the orange and red colored contour lines.



473  
 474 Figure 10. (a) Contours of the normalized sensitivity  $S^* = S/S_{max}$  as a function of pillar length  $l^*$  and characteristic  
 475 velocity  $U$  for the pillar sensor, overlaid with the plot of the evolution of  $l^*$  and  $U$  of the present pulsating flow  
 476 condition obtained from CFD simulations at the acceleration phase and the peak systole, where  $S_{max}$  is the maximum  
 477 value of the sensitivity which appears at the peak systole. (b) Plot of the normalized sensitivity relating to the shear  
 478 rate fitted by Power Curve (R-square value of 0.9981). The black circle symbols denote the selected instantaneous  
 479 values from  $0.01T_{sys}$  to  $0.21T_{sys}$  with a time increment of  $0.04T_{sys}$ , which corresponds to the instantaneous data points  
 480 ( $l^*, U$ ) shown as black circles in (a). (c) Temporal evolution of measured WS and CFD result in the calibration pulse  
 481 (sensor position  $\theta = 21^\circ$  at the inner curvature of the arch). Symbols: experiment (only every fifth point); black solid  
 482 line: CFD results; red dash line: CFD result with adapting the time-varying sensor sensitivity shown in (b).  
 483

484 Figure 10c displays exemplary the temporal WS signal for the sensor at the selected angle of  $\theta = 21^\circ$  in comparison  
 485 to the CFD result at the acceleration phase and the peak systole, i.e. the laminar phase in the flow pulse. The temporal  
 486 course of the sensor signal compared to the simulations illustrates an excellent overlap in the phase of peak systole,  
 487 while the sensor is clearly underestimating the CFD data in the ramp-up phase. This is when strong acceleration of the  
 488 bulk-flow near the entrance causes the boundary layer thickness to remain thin. By taking the sensitivity effect into  
 489 account, i.e. correcting the shear rate values obtained from CFD by multiplying with the corresponding sensor  
 490 sensitivity, we get an excellent overlap between the corrected CFD results with the values measured by the sensor.  
 491 This gives us an indication on the measurement uncertainty in certain phases of the pulsating base flow.  
 492

### 493 3.3 Sensor response

494 The relationship of the sensitivity with the wall shear rate presented in Figure 10b is further used to illustrate the  
 495 static response of the sensor. Figure 11 shows the measured tip deflection over the shear rate values from the CFD  
 496 simulations, taken during the calibration pulse. It can be seen that the initial response at weak shear-rates is non-linear  
 497 while for higher wall shear rate conditions the curve approaches a linear relationship, i.e. the range with approximately  
 498 constant gain for flow condition with high shear rate values. This static response curve is later used to transfer the  
 499 measured tip deflection to shear rate values.

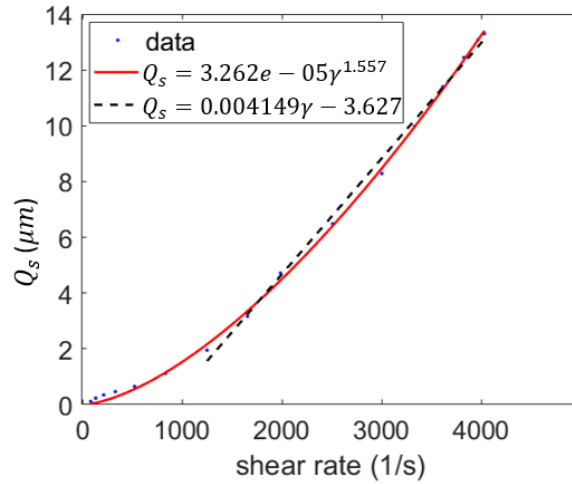
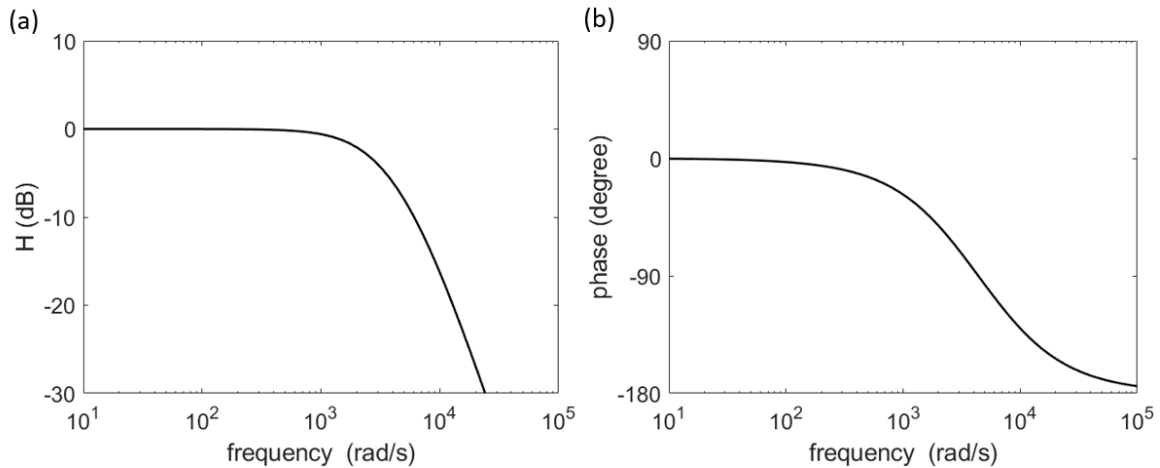


Figure 11. Static response of the micro-pillar sensor as pillar's tip displacement  $Q_s$  over the wall shear rate  $\gamma$ . The red line shows a Power Curve Fitting (R-square value of 0.9991), the black dash line shows a linear regression for the range  $1250s^{-1} \leq \gamma \leq 4000s^{-1}$  (R-square value of 0.9953).



(a) and (b) gain and phase of the sensor response, obtained from the data of the acceleration phase in Figure 10c using an input-output response analysis.

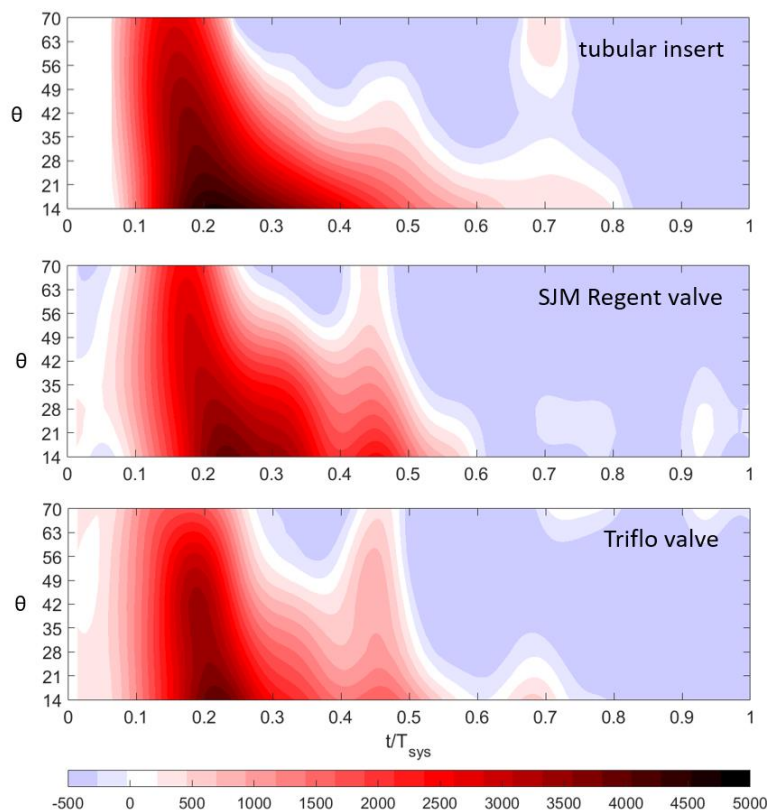
Furthermore, the curves shown in Figure 10c are used to estimate the dynamic response of the sensors (see Figure 12) with the Matlab tool "procest" with 'P2' option (MATLAB® System Identification Toolbox™)(The MathWorks). This tool estimates the parameter for the 2<sup>nd</sup> order harmonic oscillator according to Eq. (1) in the time-domain from an input-output analysis (input: sensitivity-corrected CFD values, output: experimental values). The obtained transfer functions (gain and phase) are shown in Figure 12. The best fit with 93% prediction focus provides a natural frequency of  $\omega_n = 4386.6$  rad/s and a Quality factor  $Q=0.459$ . First, the estimated natural frequency is in good agreement with the theoretical value given in section 2.1.3. Secondly, the quality factor clearly demonstrates the expected overdamped situation of the cantilever beam in the liquid environment. The response has a cut-off frequency  $f_c = 386$  Hz when the gain is at 0.7071. At a frequency of 180 Hz, the gain is still 90% of its maximum with a phase lag of  $-30^\circ$ . For frequencies below 120 Hz, the gain is better than 95% with a phase lag less than  $-20^\circ$ . This is considered the measurement range of the sensor with near constant gain and a good representation of the dynamic change of the WS.

### 3.4 Case studies

The calibrated WS sensors are then used for mapping the spatio-temporal distribution of the WS at the inner curvature of the arch in the center plane. In the following, contours of constant streamwise WS are shown in plots with time as horizontal coordinate and the angular position displayed in the vertical coordinate.

### 526 3.4.1 Systolic flow with tubular insert

527 Figure 13 shows the spatio-temporal evolution of the WS distribution at the inner curvature of the arch for the  
 528 complete systolic pulse. Because of the tubular insert (no valve), the flow is smooth and therefore also the distribution  
 529 of the WS. It can be seen that the WS reaches the absolute peak value at the entrance to the arch ( $\theta=17^\circ$ ) at the time  
 530 of peak systole ( $0.25T_{sys}$ ). However, the instant of peak WS is happening earlier in time the further we move up in the  
 531 arch; this is seen by the peak location in the time axis moving further to the left. For example, at the largest angular  
 532 position the peak occurs already at  $0.2T_{sys}$ . The first indication of flow separation is seen at the apex of the aortic arch  
 533 at  $0.28-0.3T_{sys}$  by negative WS (blue color). The separation line between forward and retrograde flow (white color)  
 534 further grows upstream over the deceleration phase along the curvature until it reaches the sinus region, which is  
 535 consistent with the flow field shown in Figure 9. Later in the cycle at about  $0.73T_{sys}$ , positive WS values re-appear in  
 536 the separated region  $56^\circ < \theta < 70^\circ$  which indicates a local flow re-attachment. In the late phase  $> 0.9T_{sys}$  the flow along  
 537 the inner curvature is retrograde all over the segment of the arch.



538 Figure 13. Spatio-temporal evolution of WS distribution along the inner curvature of the arch over the systolic flow  
 539 pulse with tubular insert (sensor calibration configuration), shown by contours of constant WS (contours from blue:  
 540 retrograde flow region with weak negative WS, to dark red: strong positive WS in streamwise direction).  
 541  
 542

### 543 3.4.2 Systolic flow with MHVs

544 The pillar sensors are applied to map the spatio-temporal evolution of streamwise WS along the inner curvature  
 545 of the aortic arch induced by different MHVs. The flow field induced by both MHVs, i.e. SJM Regent valve and Triflo  
 546 valve, has been detailed in our previous study (Li et al., 2020). The spatio-temporal evolution of the WS distribution at  
 547 the inner curvature of the arch is shown in Figure 13. Slightly negative wall shear rate values are seen at the beginning  
 548 of the systolic cycle for SJM Regent valve. This indicates that there is a backward flow along the inner curvature wall,  
 549 which may link to the opening of the SJM Regent valve when the leaflet facing the inner curvature rotates from the  
 550 valve housing to center along the hinge. This is not shown for Triflo valve because the opening of its leaflet is from  
 551 center to outside. Thereafter, a first significant peak occurs for both valves at  $0.2T_{sys}$ , the value of which is comparable  
 552 to the WS peak value generated in the calibration pulse. It indicates that this peak is induced by the wash-out flow at  
 553 the beginning of the systolic cycle. As seen from the spatio-temporal plot, the impact is rather a short-lived event as  
 554 the duration is about  $0.05T_{sys}$ . Later, a higher peak occurs for both valves at the entrance to the arch at about peak

555 systole. This is generated by the side orifice jets of the MHVs when they impact with the wall. From then on, the Triflo  
556 valve generates no further significant WS peaks, while the SJM Regent valve keeps high WS values until  $0.35T_{sys}$ . These  
557 results hint on a lower impact of the Triflo valve regarding the generation of excessive fluctuating WS stresses on the  
558 aortic wall related to the valve design. In addition, it is seen that the SJM Regent valve generates overall elevated levels  
559 of WS in the deceleration phase along the inner curvature. Clear indications of retrograde flow are found starting at  
560 the most downstream location at about  $0.5T_{sys}$ . The backflow regions with negative streamwise WS are larger extended  
561 for the SJM Regent valve compared to the Triflo valve.

#### 562 **4. Discussion**

564 Micro-pillar WSS sensors have a certain measuring range and accuracy depending on their size and flexural  
565 stiffness, besides other factors such as their sensitivity. In addition, their length relative to the thickness of the  
566 boundary layer is an important aspect affecting the measurement. As they belong to the class of indirect sensors, they  
567 need an accurate calibration under representative and repeatable flow conditions (Bruecker et al., 2007). This task  
568 may be difficult if the sensors are applied in complex geometries and/or in complex flows with oscillating boundary  
569 layers, separating flows and strongly curved streamlines. Such a situation is the pulsating flow in the aortic arch where  
570 in-vitro measurements of the WS are highly welcome to investigate the potential damage of valve-induced jets  
571 impacting with the aortic walls. An ex-situ calibration with the sensors outside the model might be not reliable for the  
572 following reasons: a) the clamping conditions of the micro-pillar at the wall can be different ex-situ and in-situ; b) the  
573 foot could be not flush with the wall, due to inaccurate assembling; c) the micro-pillar may not be perpendicular to  
574 the wall, e.g. already bent to one side; d) the shape and mechanical properties of the micro-pillar may have changed  
575 over time. All the factors mentioned above could influence the accuracy of the measuring system. Therefore, the best  
576 practice is to do the calibration in-situ in the same environment. However, even then the reference data necessary to  
577 determine the flow field around the pillars may not be easy to obtain, either from flow field measurements or from  
578 alternative measurement methods. Herein, CFD simulations are used to provide the required reference data for the  
579 calibration of the experiment in a special configuration: the aortic valve in the phantom is replaced with a tubular  
580 insert (smooth bend) and a single flow pulse is imposed, the same simulated with CFD at identical boundary conditions.  
581 An important aspect of the employed simulations is the automatic grid generation and the cost-effective laminar  
582 calculations for the acceleration part of the pulse, which make them practical for the calibration of the measurement  
583 apparatus.

584 For the calibration, the results show that the length of the sensor and the bulk flow velocity magnitude lead to a  
585 time-varying sensitivity in the situation of strong variation of mean flow with oscillating boundary layers such as in the  
586 herein studied pulsating flow. The sensitivity of the applied sensors is low in regions of thin boundary layers or to times  
587 of low velocity magnitude, whereas it increases towards a rather constant plateau for higher velocities in the range of  
588 peak systole (flow velocities 1-1.5m/s) for all relative pillar length in the span of 2-7. Excellent agreement to the  
589 measured data is found in the pulse-type calibration flow for all instants when the effect of the varying sensitivity is  
590 taken into account in the simulated data. This allowed us to determine the static and dynamic response of the sensors.  
591 With that, we can estimate the uncertainty of different length of sensors and develop design rules for best practice in  
592 using such sensors for future measurements. As a direct result of this study, we can understand why our previous  
593 measurements with 1 mm length micro-pillar sensors in the silicone model reported in (Li et al., 2020) might have  
594 resulted in overall lower WS values with potential underestimation of peak WS values of more than 50%. In addition,  
595 it cannot be excluded that the previously used silicone model had somewhat softer clamping conditions at the root of  
596 the sensors as for the Perspex model used herein. Finally, it became obvious that the material properties of the original  
597 sensors degraded over time, which requires to update the calibration data from measurements to measurement. With  
598 the methodology proposed herein, there is no need to update the reference data as the simulation conditions have  
599 not changed.

600 For the investigated heart valves the results hint on a lower impact of the Triflo valve compared to the SJM Regent  
601 regarding the generation of excessive fluctuating WS stresses on the aortic wall. In addition, it is seen that the SJM  
602 Regent valve generates overall elevated levels of WS in the deceleration phase along the inner curvature. Clear  
603 indications of retrograde flow are found starting at the most downstream location at about  $0.5T_{sys}$ . The backflow  
604 regions with negative streamwise WS are larger extended for the SJM Regent valve compared to the Triflo valve.

## 5. Conclusions

A method is presented for CFD-assisted in-situ calibration of micro-pillar WSS sensors when used for in-vitro studies of pulsating flow in the complex geometry of the aortic arch. Experimental measurements of spatio-temporal WSS maps are reported in a model of the human aorta with arrays of micro-pillar WSS sensors along the symmetry plane of the bend. The results allow quantification of the impact of heart-valve prostheses on the flow-imposed stresses along the aortic wall. A laminar flow pulse is used to calibrate the sensors in-situ with reference data from CFD simulations under equivalent boundary conditions. This method overcomes the problem of limited accuracy when the sensors are calibrated ex-situ, in other flow conditions not relevant for the current flow situation or when errors are introduced by inaccurate positioning or clamping conditions. The results show the importance of the integration effect of the length of the micro-pillar sensors, which induces uncertainties in thin boundary layers, which can be quantified now. Furthermore, the reconstructed static response allows to correct for weak sensitivities in phases of weak mean flow. Calibrated micro-pillar sensors of 500  $\mu\text{m}$  length are then employed to map the spatio-temporal evolution of WS along the inner curvature of the aorta induced by two different MHVs. It has been found that the SJM Regent valve generates higher fluctuation amplitudes of the WS for a longer duration during the systolic phase than the Triflo valve. In addition, stronger retrograde flow is generated. The results help to qualify the selection of different designs also with regards to the impact those valves have on the stresses along the aortic wall. Future measurements with the same pulse-duplicator and measurement technique allow also to address bioprostheses or transcatheter aortic valve implantation (TAVI). Furthermore, the image processing step can be converted online by using modern FPGA-based digital cameras with on-board tracking features. This would allow to track the spots of the sensor tips simultaneously and streaming the data online, while the further signal processing can be done on the fly using standard subtracting and filtering methods. With this further enhancement, the valve tester can directly visualize the impact of the heart valve on the distal walls on a display overlaid with the contours and the WS information. This represents a further step towards a more sophisticated quality control of valve design and implantation techniques using such a valve tester.

## CRedit authorship contribution statement

**Qianhui Li:** Methodology, Software, Validation, Formal Analysis, Investigation, Resources, Visualization, Data Curation, Writing – Original Draft; Writing – Review & Editing. **Evangelos Stavropoulos-Vasilakis:** Methodology, Software, Validation, Visualization, Data Curation, Writing – Original Draft. **Phoevos Koukouvini:** Supervision, Software, Writing – Review & Editing. **Manolis Gavaises:** Stewardship, Funding acquisition, Resources, Supervision, Writing – Review & Editing. **Christoph H. Bruecker:** Stewardship, Project Administration, Funding acquisition, Resources, Conceptualization, Methodology, Software, Writing – Original Draft; Writing – Review & Editing

## Acknowledgements

Prof. Bruecker holds the BAE SYSTEMS Sir Richard Olver Chair in Aeronautical Engineering and the Royal Academy of Engineering Research Chair in Nature-inspired flow sensing and manipulation. The position is co-sponsored by BAE SYSTEMS and the Royal Academy of Engineering [Grant number RCSR1617\4\11], which is gratefully acknowledged herein. The position of Dr Qianhui Li is funded by The Engineering and Physical Sciences Research Council (EPSRC) project [EP/T006315/1], which is also gratefully acknowledged herein. Dr. E. Stavropoulos-Vasilakis worked within the framework of CaFE project, which received funding from the European Union Horizon 2020 Research and Innovation programme [Grant number 642536]. The authors would like to thank Dr Andreas Papoutsakis for the thorough scientific discussion on CFD during this study, Dr Homa Naseri for the help regarding meshing strategy. The authors would also like to express our thanks to the Helmholtz Institute of RWTH Aachen University, Germany, for providing the SJM Regent valve and Novostia SA, Neuchâtel, Switzerland for the Triflo valve used in this project.

## Funding

657 This work was supported by BAE SYSTEMS and the Royal Academy of Engineering [Grant number  
658 RCSR1617\4\11], both jointly funding the position of Professor Christoph Bruecker; The position of Dr Qianhui Li is  
659 funded by The Engineering and Physical Sciences Research Council (EPSRC) project [EP/T006315/1]; Dr. E.  
660 Stavropoulos-Vasilakis worked within the framework of CaFE project, which received funding from the European Union  
661 Horizon 2020 Research and Innovation programme [Grant number 642536].  
662  
663

664 **References**

- 665 Andriotis, A., Zifan, A., Gavaises, M., Liatsis, P., Pantos, I., Theodorakakos, A., Efstathopoulos, E.P., Katritsis, D., 2008.  
666 A new method of three - dimensional coronary artery reconstruction from X - ray angiography: Validation against a  
667 virtual phantom and multislice computed tomography. *Catheterization and cardiovascular interventions* 71, 28-43.
- 668 Bodnár, T., Sequeira, A., Prosi, M., 2011. On the shear-thinning and viscoelastic effects of blood flow under various  
669 flow rates. *Applied Mathematics and Computation* 217, 5055-5067.
- 670 Borazjani, I., Ge, L., Sotiropoulos, F., 2008. Curvilinear immersed boundary method for simulating fluid structure  
671 interaction with complex 3D rigid bodies. *Journal of Computational physics* 227, 7587-7620.
- 672 Bruecker, C., Bauer, D., Chaves, H., 2007. Dynamic response of micro-pillar sensors measuring fluctuating wall-shear-  
673 stress. *Experiments in fluids* 42, 737-749.
- 674 Bruecker, C., Spatz, J., Schröder, W., 2005. Feasability study of wall shear stress imaging using microstructured  
675 surfaces with flexible micropillars. *Experiments in fluids* 39, 464-474.
- 676 Chien, S., Li, S., Shyy, J.Y., 1998. Effects of mechanical forces on signal transduction and gene expression in  
677 endothelial cells. *Hypertension* 31, 162-169.
- 678 Corso, P., Walheim, J., Dillinger, H., Giannakopoulos, G., Gülan, U., Frouzakis, C.E., Kozerke, S., Holzner, M., 2021.  
679 Toward an accurate estimation of wall shear stress from 4D flow magnetic resonance downstream of a severe  
680 stenosis. *Magnetic Resonance in Medicine*.
- 681 Dasi, L., Ge, L., Simon, H., Sotiropoulos, F., Yoganathan, A., 2007. Vorticity dynamics of a bileaflet mechanical heart  
682 valve in an axisymmetric aorta. *Physics of Fluids* 19, 067105.
- 683 De Tullio, M., Cristallo, A., Balaras, E., Verzicco, R., 2009. Direct numerical simulation of the pulsatile flow through an  
684 aortic bileaflet mechanical heart valve. *Journal of Fluid Mechanics* 622, 259-290.
- 685 Dickinson, B., Singler, J., Batten, B., 2012. Mathematical modeling and simulation of biologically inspired hair  
686 receptor arrays in laminar unsteady flow separation. *Journal of Fluids and Structures* 29, 1-17.
- 687 Dickinson, B.T., 2010. Hair receptor sensitivity to changes in laminar boundary layer shape. *Bioinspiration &*  
688 *biomimetics* 5, 016002.
- 689 Fung, Y.-c., 2013. *Biomechanics: mechanical properties of living tissues*. Springer Science & Business Media.
- 690 Gülan, U., Holzner, M., 2018. The influence of bileaflet prosthetic aortic valve orientation on the blood flow patterns  
691 in the ascending aorta. *Medical engineering & physics* 60, 61-69.
- 692 Ge, L., Dasi, L.P., Sotiropoulos, F., Yoganathan, A.P., 2008. Characterization of hemodynamic forces induced by  
693 mechanical heart valves: Reynolds vs. viscous stresses. *Annals of Biomedical Engineering* 36, 276-297.
- 694 Gross-Hardt, S., Boehning, F., Steinseifer, U., Schmitz-Rode, T., Kaufmann, T., 2018. Mesh sensitivity analysis for  
695 quantitative shear stress assessment in blood pumps using computational fluid dynamics. *Journal of biomechanical*  
696 *engineering*.
- 697 Haruguchi, H., Teraoka, S., 2003. Intimal hyperplasia and hemodynamic factors in arterial bypass and arteriovenous  
698 grafts: a review. *Journal of Artificial Organs* 6, 227-235.
- 699 Howarth, L., 1938. On the solution of the laminar boundary layer equations. *Proceedings of the Royal Society of*  
700 *London. Series A-Mathematical and Physical Sciences* 164, 547-579.
- 701 Iasiello, M., Vafai, K., Andreozzi, A., Bianco, N., 2016. Analysis of non-Newtonian effects on low-density lipoprotein  
702 accumulation in an artery. *Journal of biomechanics* 49, 1437-1446.
- 703 Iasiello, M., Vafai, K., Andreozzi, A., Bianco, N., 2017. Analysis of non-Newtonian effects within an aorta-iliac  
704 bifurcation region. *Journal of biomechanics* 64, 153-163.
- 705 Jana, A., Raman, A., Dhayal, B., Tripp, S.L., Reifenberger, R.G., 2007. Microcantilever mechanics in flowing viscous  
706 fluids. *Applied Physics Letters* 90, 114110.
- 707 Katritsis, D., Kaiktsis, L., Chaniotis, A., Pantos, J., Efstathopoulos, E.P., Marmarelis, V., 2007. Wall shear stress:  
708 theoretical considerations and methods of measurement. *Progress in cardiovascular diseases* 49, 307-329.
- 709 Katritsis, D., Theodorakakos, A., Pantos, I., Andriotis, A., Efstathopoulos, E., Siontis, G., Karcianas, N., Redwood, S.,  
710 Gavaises, M., 2010. Vortex formation and recirculation zones in left anterior descending artery stenoses:  
711 computational fluid dynamics analysis. *Physics in Medicine & Biology* 55, 1395.
- 712 Katritsis, D.G., Theodorakakos, A., Pantos, I., Gavaises, M., Karcianas, N., Efstathopoulos, E.P., 2012. Flow patterns at  
713 stented coronary bifurcations: computational fluid dynamics analysis. *Circulation: Cardiovascular Interventions* 5,  
714 530-539.

- 715 Kim, T., Cheer, A., Dwyer, H., 2004. A simulated dye method for flow visualization with a computational model for  
716 blood flow. *Journal of biomechanics* 37, 1125-1136.
- 717 Kunze, S., Chaves, H., Brücker, C., 2008. Mirror particle-tracking-velocimetry in a strip-coded light-sheet: a new  
718 method to determine the wall-shear-stress field. *Experiments in fluids* 45, 573-581.
- 719 Lantz, J., Renner, J., Karlsson, M., 2011. Wall shear stress in a subject specific human aorta—influence of fluid-  
720 structure interaction. *International Journal of Applied Mechanics* 3, 759-778.
- 721 Li, Q., Bruecker, C.H., 2018. Vortex interaction with a rough wall formed by a hexagonal lattice of posts. *Physics of*  
722 *Fluids* 30, 054107.
- 723 Li, Q., Hegner, F., Bruecker, C.H., 2020. Comparative study of wall-shear stress at the ascending aorta for different  
724 mechanical heart valve prostheses. *Journal of biomechanical engineering* 142.
- 725 Markl, M., Wallis, W., Harloff, A., 2011. Reproducibility of flow and wall shear stress analysis using flow - sensitive  
726 four - dimensional MRI. *Journal of Magnetic Resonance Imaging* 33, 988-994.
- 727 Marrero, V.L., Tichy, J.A., Sahni, O., Jansen, K.E., 2014. Numerical study of purely viscous non-Newtonian flow in an  
728 abdominal aortic aneurysm. *Journal of biomechanical engineering* 136.
- 729 Mittal, R., Simmons, S., Najjar, F., 2003. Numerical study of pulsatile flow in a constricted channel. *Journal of Fluid*  
730 *Mechanics* 485, 337-378.
- 731 Moukalled, F., Mangani, L., Darwish, M., 2016. The finite volume method in computational fluid dynamics. An  
732 Advanced Introduction with OpenFOAM and Matlab, 3-8.
- 733 Orliü, R., Vinuesa, R., 2020. Instantaneous wall-shear-stress measurements: advances and application to near-wall  
734 extreme events. *Measurement Science and Technology*.
- 735 Papathanasopoulou, P., Zhao, S., Köhler, U., Robertson, M.B., Long, Q., Hoskins, P., Yun Xu, X., Marshall, I., 2003. MRI  
736 measurement of time - resolved wall shear stress vectors in a carotid bifurcation model, and comparison with CFD  
737 predictions. *Journal of Magnetic Resonance Imaging* 17, 153-162.
- 738 Pinto, S., Romano, E., António, C., Sousa, L., Castro, C., 2020. The impact of non-linear viscoelastic property of blood  
739 in right coronary arteries hemodynamics—a numerical implementation. *International Journal of Non-Linear*  
740 *Mechanics* 123, 103477.
- 741 Politi, M.T., Ghigo, A., Fernández, J.M., Khelifa, I., Gaudric, J., Fullana, J.M., Lagrée, P.-Y., 2016. The dicrotic notch  
742 analyzed by a numerical model. *Computers in biology and medicine* 72, 54-64.
- 743 Potters, W.V., Marquering, H.A., VanBavel, E., Nederveen, A.J., 2014. Measuring wall shear stress using velocity-  
744 encoded MRI. *Current Cardiovascular Imaging Reports* 7, 9257.
- 745 Prandtl, L., 1952. *Essentials of Fluid Dynamics*, Hafner Publ. Co., New York, 117.
- 746 Raffel, M., Willert, C.E., Scarano, F., Kähler, C.J., Wereley, S.T., Kompenhans, J., 2018a. *Particle image velocimetry: a*  
747 *practical guide*. Springer.
- 748 Raffel, M., Willert, C.E., Scarano, F., Kähler, C.J., Wereley, S.T., Kompenhans, J., 2018b. *Techniques for 3D-PIV,*  
749 *Particle Image Velocimetry: A Practical Guide*. Springer International Publishing, Cham, pp. 309-365.
- 750 Raghav, V., Sastry, S., Saikrishnan, N., 2018. Experimental Assessment of Flow Fields Associated with Heart Valve  
751 Prostheses Using Particle Image Velocimetry (PIV): Recommendations for Best Practices. *Cardiovascular engineering*  
752 *and technology*, 1-15.
- 753 Shaaban, A.M., Duerinckx, A.J., 2000. Wall shear stress and early atherosclerosis: a review. *American Journal of*  
754 *Roentgenology* 174, 1657-1665.
- 755 Stankovic, Z., Allen, B.D., Garcia, J., Jarvis, K.B., Markl, M., 2014. 4D flow imaging with MRI. *Cardiovascular diagnosis*  
756 *and therapy* 4, 173.
- 757 Stettler, J., Hussain, A.F., 1986. On transition of the pulsatile pipe flow. *journal of fluid mechanics* 170, 169-197.
- 758 The MathWorks, I., *Fourier Series*, Natick, Massachusetts, United State.
- 759 The MathWorks, I., *System Identification Toolbox*, Natick, Massachusetts, United State.
- 760 Trip, R., Kuik, D., Westerweel, J., Poelma, C., 2012. An experimental study of transitional pulsatile pipe flow. *Physics*  
761 *of fluids* 24, 014103.
- 762 Tu, J., Inthavong, K., Wong, K.K.L., 2015. *Computational Hemodynamics—Theory, Modelling and Applications*.  
763 Springer.
- 764 Van Eysden, C.A., Sader, J.E., 2006. Resonant frequencies of a rectangular cantilever beam immersed in a fluid.  
765 *Journal of applied physics* 100, 114916.
- 766 Weller, H.G., Tabor, G., Jasak, H., Fureby, C., 1998. A tensorial approach to computational continuum mechanics  
767 using object-oriented techniques. *Computers in physics* 12, 620-631.

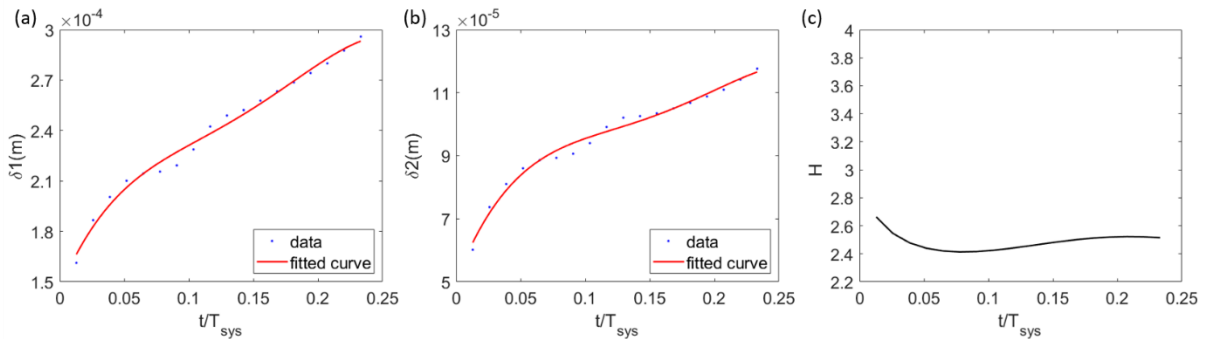
- 768 Xu, D., Warnecke, S., Song, B., Ma, X., Hof, B., 2017. Transition to turbulence in pulsating pipe flow. *Journal of Fluid*  
769 *Mechanics* 831, 418-432.
- 770 Yuce, M.I., Kareem, D.A., 2016. A numerical analysis of fluid flow around circular and square cylinders. *Journal -*  
771 *American Water Works Association* 108, E546-E554.
- 772 Zimmermann, J., Demedts, D., Mirzaee, H., Ewert, P., Stern, H., Meierhofer, C., Menze, B., Hennemuth, A., 2018. Wall  
773 shear stress estimation in the aorta: Impact of wall motion, spatiotemporal resolution, and phase noise. *Journal of*  
774 *Magnetic Resonance Imaging*.

775

776

777 **Appendices**778 **Appendix A**779 **Description of flow**

780 As shown in Figure 8a, at location  $\theta = 21^\circ$ , the boundary thickness grows from near zero to about 0.5 mm at the  
 781 very beginning of the ramp ( $t/T_{sys}=0.07$ ), about 1 mm at  $t/T_{sys} = 0.14$  and reaches a thickness of about 1.5 mm at the  
 782 peak systole; Eventually, it is growing then further due to the adverse pressure gradient in the deceleration phase. The  
 783 evolution of the boundary layer displacement thickness  $\delta_1 = \int_0^{\delta_{max}} (1 - u/U) dr$  and momentum thickness  $\delta_2 =$   
 784  $\int_0^{\delta_{max}} u/U (1 - u/U) dr$  at the acceleration phase is shown in Figure A.1a and Figure A.1b respectively, where upper  
 785 integral limit  $\delta_{max}$  is the location of the velocity peak of the instant velocity profile  $U$ . The boundary layer shape is  
 786 further quantified with the Hartree shape factor,  $H = \delta_1/\delta_2$ , of which the evolution is shown in Figure A.1c. It can be  
 787 seen that the values of the Hartree shape factor remains similar magnitude over the time with an average value of  
 788  $H = 2.5$ . According to (Dickinson, 2010),  $H = 4.029$  represents laminar separation,  $H=2.591$  corresponds to Blasius flow  
 789 (flow over a flat plate) and  $H=2.216$  indicates flow to a plane stagnation point (Hiemenz flow). It indicates that the  
 790 flow condition of the present study at the acceleration phase and the peak systole resembles the Blasius flow and  
 791 could be theoretically analyzed using Blasius solution.



792 Figure A.1. Plots of the evolution of a) the displacement boundary layer thickness  $\delta_1$ , b) the momentum boundary layer  
 793 thickness  $\delta_2$ , and c) the Hartree shape factor  $H = \delta_1/\delta_2$  over the acceleration phase obtained from CFD  
 794 simulations.  
 795

796 To analyze the sensitivity of the sensor in near wall flow with developing boundary layer, we simulate the flow  
 797 condition described by Blasius flow along a flat plate at zero incidence (Howarth, 1938) which is governed by the  
 798 Blasius equation  $f f'' + 2f''' = 0$  with the boundary conditions  $f(0) = f'(0) = 0$ ,  $f'(\infty) = 1$ .

800 The wall shear rate of Blasius flow is calculated as (Howarth, 1938)

$$801 \quad \gamma = \left(\frac{\partial u}{\partial y}\right)_{y=0} = 0.332U \sqrt{\frac{U}{\nu x}}, \quad (\text{A.1})$$

802 where  $x$  is the position from the leading edge which calculated from the Blasius solution table, using the dimensionless  
 803 coordinate  $\eta = y \sqrt{\frac{U}{\nu x}} = 5$  at  $u/U=0.99155$ .

804 We investigate on a range of values of the free stream velocity  $U$  varying from 0.01 m/s to 1.5 m/s with a step  
 805 of 0.01 m/s ; For each  $U$ , by varying the position from the leading edge, we obtained the corresponding flow profile  
 806 with a series of boundary layer thickness  $\delta_{99}$  ( $0.02 \text{ mm} \leq \delta_{99} \leq 2 \text{ mm}$ , i. e.  $0.25 \leq l^* \leq 25$ ). Thus we obtained a  
 807 series of self-similar flow profiles, which is applied to investigate on the sensitivity of the sensor, assuming that the  
 808 presence of the pillar has little effect on the surrounding upstream flow.

810 **Appendix B**811 **Rheology of Blood**

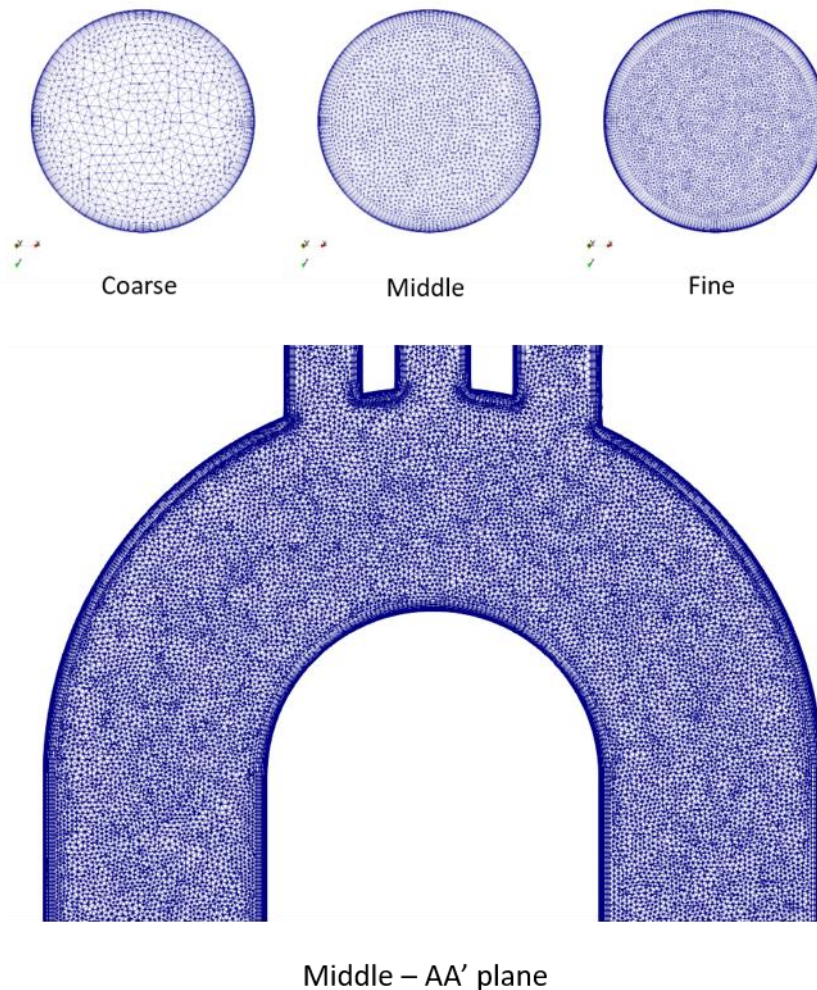
812 In the simulations the working fluid is considered Newtonian. On the one hand, this modelling strategy is followed  
 813 in order to replicate the conditions of the experiment, which is intended to provide a new kind of heart valve tester  
 814 with potential use for FDA regulation with regards to critical WSS distal of MHV. Non-Newtonian fluid effects are  
 815 expected to play a minor role for the specific problem of larger vessel studies such as the pulsatile flow through the  
 816 aorta. Numerous studies have examined the flow distribution in arteries and arterial trees, considering realistic

817 geometries derived from X-ray angiograms as well as in the carotid artery; indicative early work from the research  
818 groups (Andriotis et al., 2008; Katritsis et al., 2010; Katritsis et al., 2012) as well as more recent from Iasiello et al.  
819 (Iasiello et al., 2016, 2017) suggest that for large blood vessel dimensions such as the aorta, non-Newtonian effects  
820 play a minor role to the overall flow distribution; they become more important for smaller or stenosed vessels (Bodnár  
821 et al., 2011; Iasiello et al., 2016; Marrero et al., 2014; Pinto et al., 2020) and at time instances where recirculation  
822 zones are formed (Iasiello et al., 2016; Marrero et al., 2014) or at regions where high-velocity gradients are  
823 encountered (Pinto et al., 2020). The use of the water-glycerine mixture in the experiment and its comparison to the  
824 rheology of blood has been also discussed in our previous work (Li et al., 2020).

### 826 Grid Independence

827 An automatic unstructured tetrahedral grid generation process is chosen for the discretization of the  
828 computational domain. The inputs are limited to the CAD geometry of the aorta model and the desired cell size.  
829 Initially, the surface representing the aorta walls is triangulated; then the structured layers are created, which have a  
830 triangular base on the wall and thus, a prismatic shape; finally the volume is filled with unstructured tetrahedra.

831 In order to assess the influence of spatial resolution on the numerical calculations of the pulsatile flow under  
832 consideration and on the estimation of the WS, a grid independence study has been performed. Three different  
833 unstructured tetrahedral meshes, shown in Figure B.1, have been used with a total cell count of 2, 9 and 11 million  
834 cells, referred to as coarse, middle and fine meshes, respectively. The spatial resolution of the three meshes is listed in  
835 Table B.1. All feature additional prism layers near the wall covering the pillars, which controls better the cell height  
836 growth away from the wall and assists in better capturing the boundary layer. There are 10 layers for the coarse and  
837 medium meshes and 15 layers for the fine mesh, with a growth factor of 1.2 and a first cell height obeying the condition  
838  $y_+ \leq 1$ .



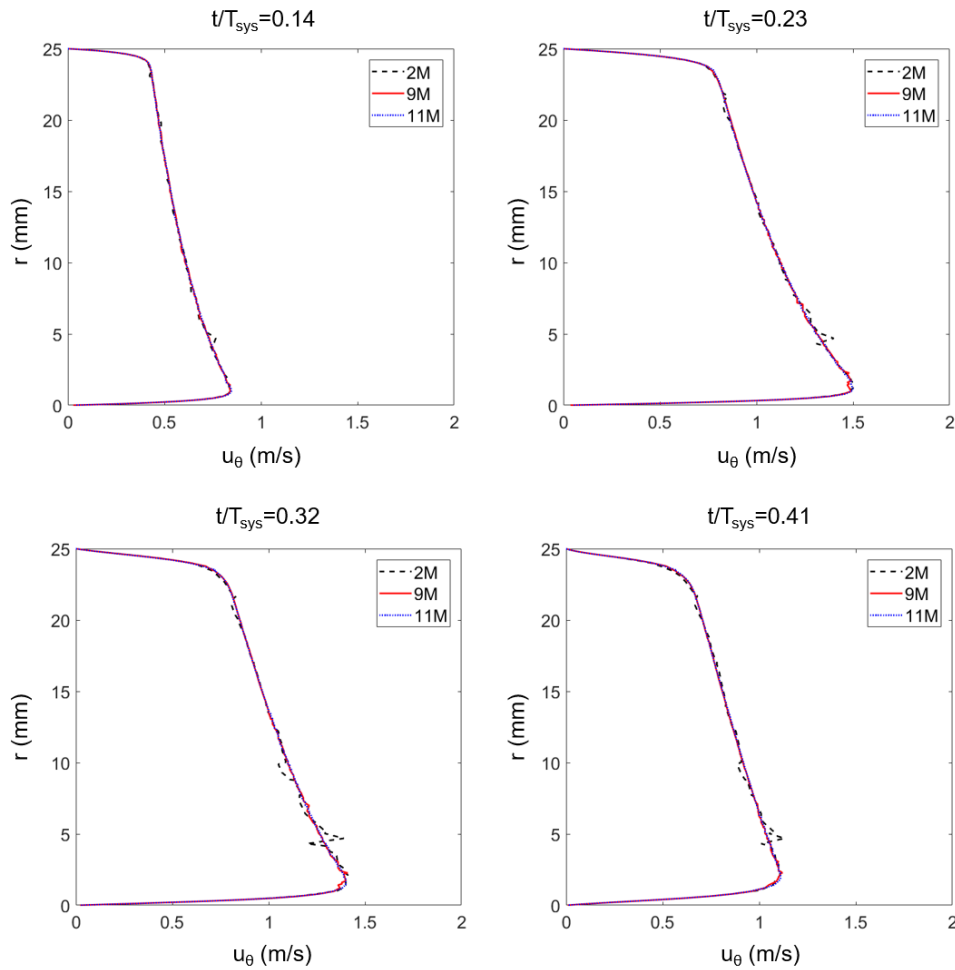
Middle – AA' plane

841 Figure B.1. Top: Cross-section slice of the mesh, on the beginning of the aorta bend ( $\theta=0^\circ$ ). Bottom: Slice on the central  
 842 plane AA' of the middle mesh, focused on the aortic arc and the roots of the arterial bifurcations. All three grids are  
 843 unstructured tetrahedral grids, with additional layers of prism cells in the near-wall region to better resolve the  
 844 boundary layer of the flow. The coarse grid is composed by 2 million cells, the medium by 9 million cells and the fine  
 845 by 11 million cells.

851 Table B.1. Resolution and computational cost of the three meshes used for the grid independence study. Along with  
 852 the total number of cells, the table shows the cell characteristic length along the aortic arc ( $dl_{arc}$ ), on the circumference  
 853 of the aorta ( $dl_{circ}$ ), in the core volume over the layers ( $h_{core}$ ) and the first cell height on the wall, with respect to the  
 854  $y_+$  rule ( $y_1/y_1^*$ ), as well as the number of nodes on the circumference of the aorta ( $N_{circ}$ ). Herein  $y_1^* = 59.4\mu m$ , for  
 855  $Re=5415$ , corresponding to the peak velocity.

Mesh Name	Cell Number	$dl_{arc}$	$dl_{circ}$	$h_{core}$	$y_1/y_1^*$	$N_{circ}$	CPUh
Coarse	2M	$D_A/42$	$D_A/21$	$D_A/63$	0.66	180	3531
Medium	9M	$D_A/57$	$D_A/44$	$D_A/97$	0.66	248	41493
Fine	11M	$D_A/77$	$D_A/63$	$D_A/120$	0.33	324	55509

857  
 858 Figure B.2 compares CFD results obtained for the three different grids. The velocity profiles along the diameter  
 859 of the aorta demonstrate convergence of the numerical predictions. Although the velocity of the bulk flow is slightly  
 860 distorted for the coarse mesh, it follows closely the results of the other grids. In conclusion, it can be argued that the  
 861 medium mesh (9 million cells) gives grid independent results for the near-wall velocity gradients along the aortic wall.  
 862



863

864 Figure B.2. Profiles of the tangential velocity  $u_\theta(r)$  in the bend corresponding to cross-section  $\theta=21^\circ$  at the centre plane.  
 865 Results for the three different grids are shown, where  $T_{sys}$  is the period of the systolic cycle.  
 866

867

**Grid generation**

868

The generation of this type of grids is fast, simple and straightforward and requires little involvement of the user. An alternative would be to use a structured hexahedral mesh, which would especially lead to a lower number of cells. However the creation of such grids, in a non-automated “blocked mesh” approach, would be challenging and importantly more time consuming. The arterial branches on top of the apex of the aorta pose a complex topological constraint to the structured hexahedral grids. Moreover, the automatic generation of a hexahedral-dominant grid may seem a promising option, however the resulting mesh may not be of great quality, especially when layering is used for the boundary layer region. The tetrahedral grid generation process employed ensures smooth transition from the structured layers to the unstructured core of the mesh. Finally, automatic hexahedral mesh generation remains a numerical challenge.

877

**Spatial resolution**

878

For pulsatile aortic flows, which usually reach a peak Reynolds of about 5,000, and where the turbulent flow is not fully developed, conventional Reynolds Averaged Numerical Simulations (RANS) modelling seems not suitable and either Large Eddy Simulations (LES) or Direct Numerical Simulations (DNS) are preferred (Mittal et al., 2003). In the current numerical investigation, laminar simulations are conducted in the acceleration phase of the pulsatile flow in the ascending region of the aortic arch, with the intension to calibrate the developed sensors. During this ramp-up part, the flow is expected to stay laminar, whereas transition in turbulence is expected later, during the deceleration phase.

884

885 The Reynolds number defined by the peak velocity of the pulse is  $Re = 5415$ , while considering the mean,  $U_m =$   
 886  $0.19 \text{ m/s}$ , it is  $Re = 1082$ , which indicate that the flow is in a transitional regime. However, for the estimation and  
 887 the assessment of the resolution of the CFD computations, one may assume that the smallest scales characterizing the  
 888 flow in a fully developed turbulent regime, can be approximated from the spatial and temporal Kolmogorov scales.  
 889 These scales are calculated as  $\eta_k = (v^3/\varepsilon)^{1/4} = 39.6\mu\text{m}$  and  $\tau_k = \sqrt{v/\varepsilon} = 0.36\text{ms}$  respectively, assuming the  
 890 dissipation rate is estimated by the peak velocity as  $\varepsilon = U_p^3/D_A = 34.3\text{m}^2/\text{s}^3$ . The same scales, calculated for the  
 891 mean velocity, with  $\varepsilon' = 0.274\text{m}^2/\text{s}^3$ , receive higher values,  $\eta_k' = 132\mu\text{m}$  and  $\tau_k' = 4\text{ms}$  respectively.

892 With regards to those scales, the middle computational mesh, features cells of size of  $11 - 14.25 \times \eta_k$  over the  
 893 wall, and  $6.25\eta_k$  in the core of the aorta, in the arch and the branches. Similarly, the coarse and fine mesh have a  
 894 resolution of  $15 - 30 \times \eta_k$  and  $8.25 - 10 \times \eta_k$  on the wall respectively, while  $10 \times \eta_k$  and  $5.25 \times \eta_k$  in the core.  
 895 Similar resolution levels have been used in computational studies of vascular flows, either in idealised or anatomic  
 896 models, found in the literature, where structured meshes are employed and the average cell size can be estimated  
 897 around  $3 - 4 \times \eta_k$  (Borazjani et al., 2008; Dasi et al., 2007; De Tullio et al., 2009; Ge et al., 2008). Therefore, the  
 898 resolution of the fine grid seems able to correctly resolve the features of the flow. The good agreement between the  
 899 results of the middle grid and the experimental PIV data at peak systole, presented in previous section, as well as the  
 900 convergence on the predictions of middle and fine grids, strongly suggest that further refinement of the mesh would  
 901 not alter the results.

902 Denser grids, would assert that fully resolved DNS computations are performed, however they would require  
 903 significantly more computational power. As it can be seen from the last column of Table B.2, where the computational  
 904 cost of the simulation of the entire pulse is given, the computations are demanding and the required resources  
 905 increase rapidly with the enhancement of the spatial resolution. While the computations on the coarse grid are  
 906 feasible on a workstation equipped with a multi-thread processor, the fine grid calculations require a multi-processor  
 907 cluster. It has to be noted that the simulation past the peak systole, is more demanding because of the higher velocities  
 908 and the more complex flow structures that have been developed. A fully resolved DNS computation on a similar grid  
 909 with average cell size of  $4 \times \eta_k$ , would cost more than 2 times what the fine mesh costed, while a model discretised  
 910 by a homogeneous grid with cell size of  $\eta_k$ , would increase exponentially the cost. On the other hand, while  
 911 Kolmogorov scales govern the resolution of DNS calculations, the Taylor spatial micro-scale, which can be estimated  
 912 as  $\lambda = \sqrt{10} \cdot Re_{U_p}^{-1/2} \cdot D_A = 1.1\text{mm}$ , is relevant to LES computations. It can be seen that the size of a mesh  
 913 accommodating this scale, which is approximately 20 times greater than the equivalent Kolmogorov scale, would be  
 914 between the size of the coarse and the middle mesh used herein, and the resources needed would be equivalent or  
 915 higher than those needed for the middle mesh. As a reference, the computational cost of a test simulation of a bileaflet  
 916 MHV on a 2.5 million cells unstructured tetrahedral mesh, following a similar laminar approach needed 6600 CPUh  
 917 only up to peak systole, while when employing LES the cost jumped to 7600 CPUh. Thus, for the purposes of in-situ  
 918 calibration of the WS sensors, the process followed in the current study, which combines the fast and automatic grid  
 919 generation with laminar numerical simulations, seems more appropriate.